

STRUCTURE FORMING PROCESSES IN  
MESOSCOPIC POLYMER SYSTEMS

by

TOMAS KOCI

(Under the direction of Michael Bachmann)

ABSTRACT

This is going to be the best abstract ever :)

INDEX WORDS: Polymer Aggregation, Monte Carlo Simulations, Parallel Tempering,  
Multicanonical Sampling, Canonical Analysis, Microcanonical  
Inflection-Point Analysis, Flexible Polymer, Structural Transitions,  
Finite Systems, Finite-Size Effects

STRUCTURE FORMING PROCESSES IN  
MESOSCOPIC POLYMER SYSTEMS

by

TOMAS KOCI

B.A., The Juilliard School, 2008

A Dissertation Submitted to the Graduate Faculty  
of The University of Georgia in Partial Fulfillment  
of the

Requirements for the Degree

DOCTOR OF PHILOSOPHY

ATHENS, GEORGIA

2016

©2016

Tomas Koci

All Rights Reserved

STRUCTURE FORMING PROCESSES IN  
MESOSCOPIC POLYMER SYSTEMS

by

TOMAS KOCI

Approved:

Major Professor: Michael Bachmann

Committee: Steven P. Lewis  
Heinz-Bernd Schuttler

Electronic Version Approved:

Alan Dorsey  
Dean of the Graduate School  
The University of Georgia  
July 2016

# Acknowledgments

# Contents

Acknowledgments	iv
List of Figures	xiii
List of Tables	xiv
<b>1 Introduction</b>	<b>1</b>
<b>2 Elements of Statistical Mechanics</b>	<b>2</b>
2.1 The microcanonical ensemble . . . . .	3
2.2 The canonical ensemble . . . . .	10
2.3 Alternative definitions of the density of states . . . . .	17
<b>3 Computational Methods</b>	<b>25</b>
3.1 Markov chain Monte Carlo . . . . .	26
3.2 Histogram reweighting methods . . . . .	33
3.3 Simple Monte Carlo updates . . . . .	37
<b>4 Off-Lattice Polymer Models</b>	<b>40</b>
4.1 Coarse-grained models . . . . .	41
4.2 Flexible elastic homopolymer . . . . .	43
4.3 Structural order parameters . . . . .	47

<b>5</b>	<b>Confinement Effects upon Structural Transitions in Elastic Polymer Chains</b>	<b>50</b>
5.1	Model and simulation parameters . . . . .	51
5.2	Results . . . . .	53
5.3	Summary . . . . .	63
<b>6</b>	<b>Impact of Bonded Interactions on the Ground-State Geometries of Flexible Homopolymers</b>	<b>65</b>
6.1	Model and Methods . . . . .	65
6.2	Results . . . . .	68
6.3	Summary . . . . .	73
<b>7</b>	<b>Aggregation of Flexible Elastic Homopolymers</b>	<b>76</b>
7.1	Introduction . . . . .	76
7.2	Microcanonical analysis . . . . .	76
<b>8</b>	<b>Summary and Outlook</b>	<b>77</b>
	<b>Bibliography</b>	<b>77</b>

# List of Figures

2.1	Microcanonical inflection-point analysis of the inverse microcanonical temperature $\beta(E)$ . The prominent back-bending region in $\beta(E)$ , together with the positive-valued peak in its energy derivative $\gamma(E)$ at $E \approx -15$ , indicates a first-order transition. The negative-valued peak at $E \approx -24$ corresponds to a second-order transition. . . . .	7
2.2	The convex region of the microcanonical entropy $S(E)$ and the back-bending of the microcanonical inverse temperature $\beta(E)$ are prominent indicators of <i>first-order</i> transitions. The slope of the double-tangent Gibbs hull $\mathcal{H}(E)$ defines the transition temperature $\beta_{\text{tr}}$ . The Maxwell construction, defined by equal areas of $s_o$ and $s_d$ , is itself positioned at $\beta_{\text{tr}}$ . The transition energy $E_{\text{tr}}$ indicates the location of the largest separation between $\mathcal{H}(E)$ and $S(E)$ , which signifies maximal entropic suppression of the transition states. The latent heat $\Delta Q$ corresponds to the width of the transition region between $E_d$ and $E_o$ . . . . .	8
2.3	(a) The jump discontinuity in the canonical entropy $S$ , (b) and the delta peak in the specific heat $C_V$ , are characteristic of a first order phase transition. . .	13



2.4	Second order transitions are characterized by discontinuities in response quantities, such as the specific heat. (a,b) In the case of a <b>critical</b> second order transition, the entropy $S$ attains an infinite slope at $T_c$ accompanied by a divergence in the specific heat $C_V$ . (c,d) So called <i>lambda</i> transitions are characterized by a jump discontinuity in $C_V$ and a cusp singularity in entropy.	14
2.5	(a) The peak in the specific heat $C_V$ indicates a region of heightened thermodynamic activity. (b) The two peaks in the bimodal canonical energy distribution correspond to the ordered and disordered pseudophases, energetically separated by the latent heat $\Delta Q$ . Pseudophase coexistence and latent heat are reliable indicators of a first-order pseudophase transition. (c) Second-order transitions are marked by wide unimodal energy distributions at the transition point.	16
2.6	Results of a Monte Carlo simulation of a short flexible homopolymer of length $N = 13$ . The average kinetic energy $\langle E_k \rangle$ and the kinetic contributions $C_{V,\text{kin}}$ towards the specific heat are plotted as points on top of their respective theoretical curves (blue). The average potential energy $\langle E_c \rangle$ and the configurational specific heat $C_{V,\text{conf}}$ (green) were obtained by sampling of the configurational space. Sampling of the full phase space was performed to obtain the total average energy $U$ and the combined specific heat $C_V$ (red). As expected, the combined specific heat is identical to $C_{V,\text{conf}}$ , except for a trivial additive constant.	20

2.7	Comparison of microcanonical results from a Monte Carlo simulation of a flexible homopolymer of length $N = 55$ . (a) The combined $S$ , conformational $S_c$ , and kinetic $S_k$ entropy curves. (b) The kinetic inverse temperature $\beta_k$ is a strictly convex function and the application of the inflection-point analysis reveals no transition signals. The conformational inverse temperature $\beta_c$ clearly differs from $\beta(E)$ , however both indicate a first-order pseudophase transition at virtually the same temperature. . . . .	23
2.8	Comparison of the inverse microcanonical temperature $\beta(E)$ (red) and the conformational inverse temperature $\beta_c(\bar{E}_p)$ (blue) evaluated at the most probable potential energy $\bar{E}_p$ . The approximation introduced in equation 2.41 holds except in the back-bending region of the first-order pseudophase transition. The inverse transition temperature $\beta_{\text{trans}}$ obtained from the two quantities is virtually identical. . . . .	24
3.1	Canonical and GME energy histograms at a first-order pseudophase transition. The bimodal canonical energy histogram indicates the coexistence of ordered and disordered pseudophases, separated by an entropically suppressed energy region. Each GME ensemble enhances the sampling of suppressed states over a limited energy range. . . . .	32
3.2	(a) Illustration of the canonical energy histograms $h(E, \beta_i)$ , (b) the individual estimates of the logarithm of the density of states $\bar{S}_i(E)$ , (c) and the combined estimate of the logarithm of the density of states $\hat{S}(E)$ obtained by reweighting. . . . .	34
3.3	Comparison between the noisy derivative of the microcanonical inverse temperature $\gamma(E) = d\beta/dE$ and the Beziér approximation $\gamma_{\text{bez}}(E)$ . The systematic error in the Beziér approximation is visible near $E_{\text{trans}}$ , where the curvature of $\gamma(E)$ changes abruptly. . . . .	36

3.4	Example of a distribution of the temperature dependent displacement parameter $l(T)$ , used in a parallel tempering simulation of a flexible elastic 55-mer. The values of $l(T)$ were selected to keep the average acceptance rates $\langle a \rangle$ within the optimal range of $\sim 30\% - 70\%$ . . . . .	38
3.5	Schematic depiction of the single-displacement and the rotational pivot updates. In a displacement update, a randomly selected monomer is moved according to a randomly generated displacement vector $\Delta \mathbf{r}_i$ . The pivot update consists of rotating a portion of the polymer chain over a randomly chosen axis $\mathbf{k}$ by a random angle $\Delta \phi$ . . . . .	39
4.1	An example of a coarse-grained model of polyethylene. Methylene groups ( $\text{CH}_2$ ) are replaced by coarse-grained interaction sites which are depicted as transparent spheres. The interactions between the sites are described in terms of effective potentials. . . . .	41
4.2	(a) Non-bonded interactions in the generic model of an elastic homopolymer are represented by the Lennard-Jones potential. Interacting monomers experience strong repulsion below the equilibrium distance $r_0$ , and are weakly attracted over the interval $(r_0, r_c)$ where $r_c$ marks the cutoff distance. (b) The nonlinear FENE potential (red) is a symmetric representation of the bonded interactions. As a possible variant, the symmetry of the bonded potential can be broken by combining the FENE and the Lennard-Jones potentials (green). . . . .	44
4.3	(a) Generic model of a flexible elastic homopolymer. All monomers interact via a pairwise Lennard-Jones potential (LJ). Bonded interactions include an additional finitely extensible nonlinear elastic potential (FENE). (b) In a multi-chain system, the interactions between monomers belonging to different chains are also represented by the (LJ) potential. . . . .	45

4.4	The thermal fluctuations of the radius of gyration obtained from a Monte Carlo simulation of an elastic 55mer. The distinct peaks indicate the locations of the freezing and collapse transitions at the temperatures $T_{\text{freezing}}$ and $T_{\text{collapse}}$ respectively. . . . .	48
4.5	Intensity plots of the rotationally invariant order parameter $Q_6$ for two variants of a coarse-grained model of an elastic 15mer. The shading indicates the probability of detecting a configuration with a given value of the order parameter, red being the maximum probability and black being the lowest. In figure (a), the two prominent low energy branches reveal the existence of two solid pseudophases with distinct conformational geometries. Whereas in (b), only a single solid phase is detected. . . . .	49
5.1	Behavior of the combined bond potential $U_{\text{bonded}}(r_{ii+1}) = U_{\text{LJ}}(r_{ii+1}) + U_{\text{FENE}}(r_{ii+1})$ for different values of the effective bond confinement range $R$ . . . . .	52
5.2	Specific heat and the thermal fluctuations of the radius of gyration for 13mers and 30mers, parametrized by the bond confinement parameter $R$ . . . . .	55
5.3	Energy histograms of the 13mer with $R = 15$ at several temperatures near the $\Theta$ point. The bimodal shape of the histograms near the transition temperature $T_\theta = 0.331$ clearly indicates a first order pseudophase transition. . . . .	57
5.4	Structural phase diagrams for 13mers and 30mers, parametrized by the canonical temperature $T$ and the confinement parameter $R$ . The blue (solid) and pink segments indicate first-order-like and second-order-like transitions, respectively. . . . .	59

5.5	Microcanonical results for 13mers with bond confinement ranges (a) $R = 0.3$ , (b) 4.5, and (c) 30 as well as for 30mers (d)-(f). Shown are inverse temperature curves $\beta(E)$ , their first derivatives $\gamma(E) = d\beta(E)/dE$ , and (on arbitrary scale) the energy histograms $h(E)$ at the $\Theta$ transition temperature. The horizontal dashed line marks $\gamma = 0$ . The positive valued peaks of $\gamma(E)$ for values of $R > 4.5$ clearly indicate that the $\Theta$ transition is first order, but remains separate from the freezing transition. The absorption of the freezing transition by the $\Theta$ transition is apparent for large confinement ranges (c, f). . . . .	61
6.1	The modified bonded potential $U_B(r)$ , modeled by the FENE and LJ interactions. The strength of the Lennard-Jones term is controlled by the bond flexibility parameter $\eta \in [0, 1]$ . . . . .	67
6.2	(a) Heat capacity $C_v$ , (b) microcanonical inverse temperature $\beta(E)$ , and (c,d) its first and second derivatives $\gamma(E)$ and $\delta(E)$ , respectively. . . . .	69
6.3	(a) Microcanonical hyper-phase diagram parametrized by energy and the bond flexibility control parameter $\eta$ . Here, G, L, and S stand for “gas”, “liquid”, and “solid” structural phases, respectively. The $S_{\text{ic-core}}$ pseudophase consists mostly of incomplete icosahedral structures. $S_{\text{ic}}$ and $S_{\text{bi}}$ incorporate compact icosahedral and bihexagonal structures, respectively. (b) Enlarged section detailing the low energy region for $\eta < 0.15$ . The solid-solid transition line is extended by a dashed empirical line constructed based on the data provided by structural analysis. . . . .	71

6.4	(a,b,c,d) Intensity plots of the $Q_6$ order parameter for a 15mer with $\eta = 0.00, 0.05, 0.10, 1.0$ . The shading indicates the probability of detecting a configuration with a given value of the order parameter, red being the maximum probability and black being the lowest. The freezing and the solid-solid transitions are indicated by solid and dashed horizontal lines respectively. For $\eta \leq 0.1$ , the polymer has two distinct solid phases. In addition to the icosahedral phase ( $Q_6 \approx 0.65$ ) the polymer is found in the bihexagonal phase at low energies ( $Q_6 \approx 0.41$ ). . . . .	74
6.5	Two distinct low-energy structures of the elastic 15-mer. (a) Compact structure with a stable icosahedral core and two monomers displaced onto the incomplete second layer. (b) The bihexagon is the preferred ground-state geometry for $\eta \leq 0.1$ . . . . .	75

# List of Tables

5.1	Microcanonical transition temperatures $T_{\text{f},\theta}$ and latent heats $\Delta q_{\text{f},\theta}$ at the freezing and $\Theta$ transition points, respectively, for 13mers with different bond confinement ranges $R$ . . . . .	63
5.2	Same as Table 5.1, but for 30mers. 63	
8.1	Example of a table. . . . .	77

# Chapter 1

## Introduction

Kickass intro...



# Chapter 2

## Elements of Statistical Mechanics

Statistical mechanics aims at explaining the microscopic origins of macroscopic properties of systems with large numbers of degrees of freedom. The exact solution for the time evolution of every particle in a single complex system requires enormous computational efforts, and in most cases provides little insight. In contrast to the stochastic motion of microscopic particles in a thermal environment, collective system properties such as entropy, pressure, or temperature, for the most part exhibit relatively simple behavior. The formalism of statistical mechanics allows us to study these properties by considering the average behavior of a large number of identically prepared systems, i.e., the statistical ensemble. It is well established, that for very large systems near the thermodynamic limit, all ensembles become equivalent. However this is emphatically not true in the case of intrinsically finite systems for which the choice of an ensemble is non-trivial [1]. Therefore, we shall briefly introduce several prominent statistical ensembles, starting with arguably the most fundamental one, the *microcanonical ensemble*.

## 2.1 The microcanonical ensemble

Let us consider a mechanically and adiabatically isolated system with a constant number of particles ( $N$ ), volume ( $V$ ), and energy ( $E$ ). At any given moment, the system is to be found in a particular microstate  $\mu$ , which is represented by a point in a  $6N$  dimensional phase-space. At a fixed energy  $E$ , the accessible microstates are constrained to the surface of constant energy  $\mathcal{H}(\mu) = E$ , where  $\mathcal{H}$  is the Hamiltonian of the system. The total number of microstates corresponding to a macrostate with a fixed energy  $E$  is obtained by calculating the density of states<sup>1</sup>

$$g(E) = \int \mathcal{D}\mathcal{P}\mathcal{D}\mathcal{Q} \delta(E - \mathcal{H}(\mathcal{P}, \mathcal{Q})), \quad (2.1)$$

where

$$\mathcal{D}\mathcal{P}\mathcal{D}\mathcal{X} = \prod_{n=1}^N \frac{d^3 p_n d^3 x_n}{(2\pi\hbar)^3} \quad (2.2)$$

is the Lebesgue measure over phase space [2]. In computational studies, the energy space is by necessity discretized into intervals of width  $\Delta E$ , and the density of states  $g(E_i)$  is obtained by counting the microstates within a thin shell of width  $\Delta E$ . Formally,  $g(E_i)$  is a discrete function defined as

$$g(E_i) = \int_{E_i - \Delta E/2}^{E_i + \Delta E/2} g(E) dE, \quad (2.3)$$

where  $g(E)$  in the integrand is the continuous density of states [1].

Assuming that no additional quantities are conserved, i.e. the system is ergodic, all accessible microstates have equal a priori probabilities [3]. The microcanonical equilibrium probability distribution is given by

$$p(\mu)_E = \begin{cases} 1/g(E), & \text{if } \mathcal{H}(\mu) = E \\ 0, & \text{if } \mathcal{H}(\mu) \neq E, \end{cases} \quad (2.4)$$

---

<sup>1</sup>Please refer to section 2.3 for detailed discussion of alternative definitions of the density of states.

and the expectation value of an observable  $O$  at a fixed energy  $E$  is found by averaging over the surface of constant energy

$$\langle O \rangle_E = \int \mathcal{D}\mathcal{P} \mathcal{D}\mathcal{Q} \ O(\mathcal{P}, \mathcal{Q}) \ \delta(E - \mathcal{H}(\mathcal{P}, \mathcal{Q})). \quad (2.5)$$

The density of states of a typical mesoscopic system can easily span several thousands of orders of magnitude. It is therefore convenient to define the microcanonical equilibrium entropy

$$S(E) = k_B \ln g(E), \quad (2.6)$$

as an *extensive* quantity with dimensions of energy over temperature.<sup>2</sup>

### 2.1.1 Microcanonical temperature

Temperature is one of the most fundamental concepts of statistical mechanics. Traditionally, it has been defined in terms of average kinetic energies of particles in a system [4]. In the following, we wish to motivate a more fundamental definition and introduce temperature as an intrinsic system property which can be obtained directly from the microcanonical density of states. For this purpose, let us consider an adiabatically isolated system composed of two weakly interacting subsystems,  $S_1$  and  $S_2$ . The energy of the combined system is constant and can be written as the sum of the energies of the two subsystems  $E = E_1 + E_2$ . At a fixed system energy  $E$ , the probability density for subsystem  $S_1$  to contain energy  $E_1$  is written as

$$\rho(E_1)_E = \frac{g_1(E_1)g_2(E - E_1)}{g(E)}. \quad (2.7)$$

---

<sup>2</sup>If temperature is measured in the more natural units of energy, entropy becomes a unitless quantity and the Boltzmann constant equals to unity.

The density of states of the combined system is given by the convolution of the subsystem densities

$$g(E) = \int dE_1 g_1(E_1) g_2(E - E_1). \quad (2.8)$$

In systems with many degrees of freedom, the probability density  $\rho(E_1)_E$  is a sharply peaked distribution around the equilibrium energy  $\bar{E}_1$ <sup>3</sup>. Hence the convolution in Eq. 2.8 can be well approximated by the maximum value of the integrand [5]. The maximum is found when the derivative of the integrand with respect to  $E_1$  is set to zero. It follows that

$$\left. \frac{1}{g_1} \frac{dg_1}{dE_1} \right|_{\bar{E}_1} = \left. \frac{1}{g_2} \frac{dg_2}{dE_2} \right|_{E-\bar{E}_1}, \quad (2.9)$$

or alternatively in terms of the microcanonical entropy

$$\left. \frac{dS_1}{dE_1} \right|_{\bar{E}_1} = \left. \frac{dS_2}{dE_2} \right|_{E-\bar{E}_1}. \quad (2.10)$$

In analogy to the familiar observation that interacting systems at thermal equilibrium have equal temperatures, we define the microcanonical temperature as

$$T(E) = \left( \frac{dS(E)}{dE} \right)^{-1}. \quad (2.11)$$

Frequently, it is more convenient to consider instead the inverse microcanonical temperature

$$\beta(E) = \frac{dS(E)}{dE}. \quad (2.12)$$

---

<sup>3</sup>The energy fluctuations per particle around the equilibrium energy  $\bar{E}_1$  scale as  $N^{-1/2}$  [5].

### 2.1.2 Microcanonical analysis of phase transitions

A macrostate of a system is specified by a set of macroscopic variables and possesses the characteristics of the predominant microstates. Macrostates are said to belong to the same thermodynamic phase, if in a given range of some external control parameters<sup>4</sup> all of the system's thermodynamic observables are analytic, i.e. have convergent Taylor expansions. Singularities in the observables signify the presence of phase transitions between distinct phases, typically marked by abrupt changes in macroscopic properties in response to minute variations of external control parameters. Phase transitions can be roughly divided into two categories. *Abrupt* transitions are characterized by the coexistence of two distinct phases and discontinuities in most physical properties. *Continuous* transitions, although less common in nature, have been the object of most intense research. They are marked by diverging correlation lengths, large fluctuations, and scale invariance [5].

Divergences and singularities in thermodynamic observables and their derivatives are only found in systems which satisfy the thermodynamic limit. In mesoscopic systems<sup>5</sup>, due to finite size effects, divergences are replaced by peaks and discontinuities are smoothed over [1]. For clarity, we designate the term *pseudophase transition* to represent significant conformational changes in finite systems. Likewise, thermodynamic phases in finite systems shall be referred to as *pseudophases*. In the following, we present a powerful formalism for the analysis of pseudophase transitions in the microcanonical ensemble; the microcanonical inflection point analysis.

---

<sup>4</sup>Some common examples of external control parameters are the canonical temperature, pressure, or the chemical potential.

<sup>5</sup>Typical length scales in mesoscopic systems are of the order of  $\sim 10^3$  nanometers. In this regime, exact quantum many-body interactions can be replaced by effective classical potentials, and cooperative effects dominate structure formation processes. Mesoscopic systems are distinct from macroscopic systems due to the presence of significant finite-size effects, which disallow the simplifying assumptions of the thermodynamic limit.

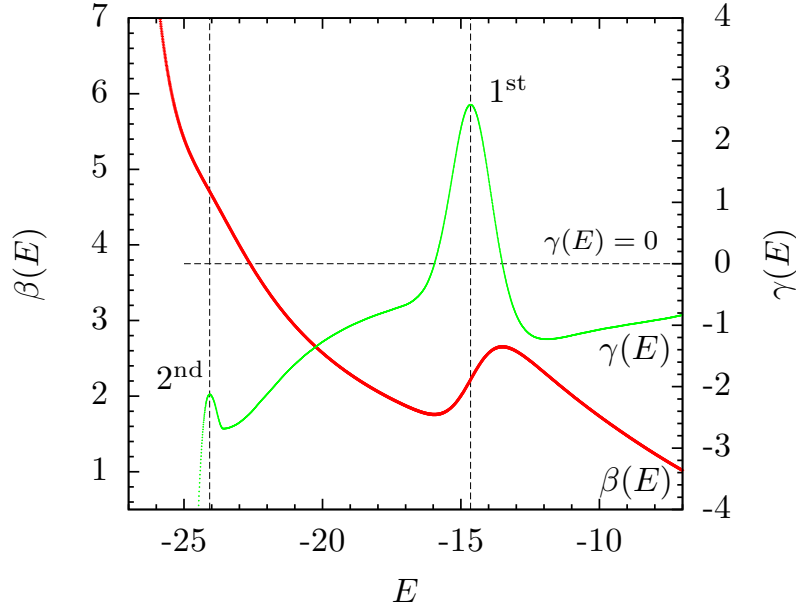


Figure 2.1: Microcanonical inflection-point analysis of the inverse microcanonical temperature  $\beta(E)$ . The prominent back-bending region in  $\beta(E)$ , together with the positive-valued peak in its energy derivative  $\gamma(E)$  at  $E \approx -15$ , indicates a first-order transition. The negative-valued peak at  $E \approx -24$  corresponds to a second-order transition.

### Microcanonical inflection-point analysis

Unlike its canonical counterpart – the heat-bath temperature – the microcanonical inverse temperature is an inherent property of the system, derived directly from the fundamental microcanonical quantities  $S(E)$  and  $E$ . We assert that all essential information about energetically and entropically driven thermodynamic processes is contained in its curvature. Hence the microcanonical inverse temperature is an ideal starting point for a comprehensive analysis of pseudophase transitions [6].

In analogy to the principle of minimal sensitivity [7], structural transitions between pseudophases occur when  $\beta(E)$ , or one of its energy derivatives, respond least sensitively to variations in energy [8]. In particular, first-order transitions are associated with inflection

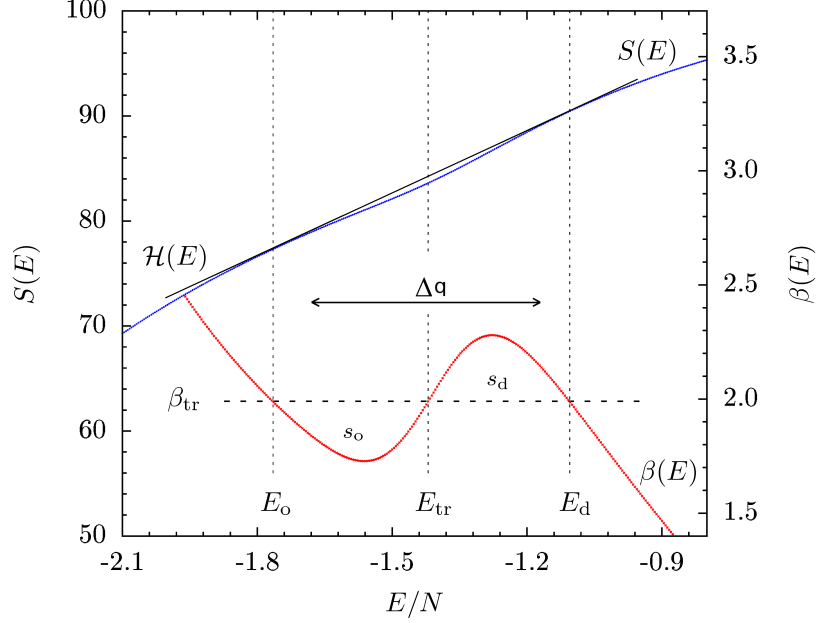


Figure 2.2: The convex region of the microcanonical entropy  $S(E)$  and the back-bending of the microcanonical inverse temperature  $\beta(E)$  are prominent indicators of *first-order* transitions. The slope of the double-tangent Gibbs hull  $\mathcal{H}(E)$  defines the transition temperature  $\beta_{\text{tr}}$ . The Maxwell construction, defined by equal areas of  $s_o$  and  $s_d$ , is itself positioned at  $\beta_{\text{tr}}$ . The transition energy  $E_{\text{tr}}$  indicates the location of the largest separation between  $\mathcal{H}(E)$  and  $S(E)$ , which signifies maximal entropic suppression of the transition states. The latent heat  $\Delta Q$  corresponds to the width of the transition region between  $E_d$  and  $E_o$ .

points in  $\beta(E)$  that have a positive slope, accompanied by positive-valued peaks in the energy derivative  $\gamma(E) = d\beta(E)/dE$ . Similarly, a second-order transition occurs when  $\beta(E)$  exhibits an inflection point with a negative slope and  $\gamma(E)$  attains a negative-valued peak. Examples of microcanonical pseudophase transition signals are shown in Fig. 2.1. The formalism can be naturally extended to higher-order transitions. Inflection point in the  $(2n)$ th-derivative of entropy, accompanied by a positive-valued valley in the  $(2n + 1)$ th-derivative, indicates a  $(2n + 1)$ th-order transition. Similarly, a  $(2n)$ th-order transition is marked by an inflection point in the  $(2n - 1)$ th-derivative of entropy and a negative-valued peak in the  $(2n)$ th-order derivative.

Alternatively, in the case of first-order transitions, the transition temperature  $\beta_{\text{tr}}$  can be obtained by the means of the Maxwell construction which was originally introduced to repair the unphysical back-bending in the pressure versus volume isotherms for the van der Waals gas. In mesoscopic systems, the finite-size effects lead to the entropic suppression of transition states, which is manifested in the backbending of  $\beta(E)$  and the convex intruder in  $S(E)$ . The position of the Maxwell construction is determined by the equality of the areas  $s_o$  and  $s_d$  [Fig.2.2]. Commonly referred to as *surface entropies*,  $s_o$  and  $s_d$  are defined as the integrals

$$s_o = \int_{E_o}^{E_{\text{tr}}} dE (\beta_{\text{tr}} - \beta(E)), \quad (2.13)$$

$$s_d = \int_{E_{\text{tr}}}^{E_d} dE (\beta(E) - \beta_{\text{tr}}). \quad (2.14)$$

The Maxwell line intersects the inverse temperature at the energies  $E_o$ ,  $E_{\text{tr}}$ , and  $E_d$ . The latent heat  $\Delta Q = E_d - E_o$  corresponds to the energetic separation between the ordered and the disordered pseudophases. The transition energy  $E_{\text{tr}}$  indicates the location where intermediate states experience the maximal entropic suppression [1].

The slope of the double-tangent Gibbs construction, also shown in Figure 2.2, provides yet another definition of  $\beta_{\text{tr}}$ . As a function of energy, the Gibbs hull is defined as

$$\mathcal{H}(E) = S(E_o) + \beta_{\text{tr}}[E - E_o], \quad (2.15)$$

where  $\beta_{\text{tr}}$  can be expressed in terms of the energy and entropy differences between the ordered and disordered pseudophases as

$$\beta_{\text{tr}} = \frac{S_d - S_o}{E_d - E_o} = \frac{\Delta S}{\Delta Q}. \quad (2.16)$$



With the exception of composite multi-step transitions, characterized by additional oscillations in the back-bending region of  $\beta(E)$ , the transition temperatures obtained by the means of the Maxwell and Gibbs constructions are identical.

The formalism of the microcanonical inflection-point analysis makes no reference to the thermodynamic limit. In fact, it is equally suitable for analysis of macroscopic and mesoscopic systems alike. This is in stark contrast to the more traditional canonical analysis which is defined under the assumption of the thermodynamic limit and has to be modified for the treatment of finite systems.

## 2.2 The canonical ensemble

The canonical ensemble describes the behavior of a closed system which is in thermal equilibrium with a large external heat bath at a fixed temperature  $T$ . In analogy to the density of states in the microcanonical ensemble, the partition function  $Z(T)$  contains all the essential information about the thermodynamic properties of the system under consideration [9]. It can be defined directly as a Laplace transform<sup>6</sup> of the microcanonical density of states  $g(E)$

$$Z(T) = \sum_i g(E_i) e^{-\frac{E_i}{k_B T}}, \quad (2.17)$$

where  $T$  is the canonical temperature and  $k_B$  is the Boltzmann constant. The condition of thermal equilibrium prohibits any net average energy transfer between the system and the heat bath. However, the system can temporarily gain or lose energy through constant fluctuations and dissipations. The probability for a given microstate  $\mu$  at a temperature  $T$

---

<sup>6</sup>Here we assume that the system under investigation has discrete energy levels, which is always true in the context of computational studies. In the case of a continuous energy spectrum, the discrete sum is replaced by the integral  $Z(T) = \int dE g(E) e^{-\frac{E}{k_B T}}$ .

is given by the Boltzmann distribution

$$p(\mu) = \frac{1}{Z(T)} e^{-\frac{\mathcal{H}(\mu)}{k_B T}}, \quad (2.18)$$

where  $\mathcal{H}$  is the Hamiltonian of the system. The appropriate thermodynamic potential in the canonical ensemble is the Helmholtz free energy

$$F(T) = -k_B T \ln Z(T). \quad (2.19)$$

This quantity represents the energy available to perform work and can be used to obtain all other thermodynamic quantities by differentiation [4, 5]. The temperature derivative of the free energy defines the canonical entropy

$$S(T) = -\frac{\partial}{\partial T} F(T) \Big|_{N,V}, \quad (2.20)$$

which measures the amount of disorder in the system. The internal energy  $U$ , defined as a sum over all microstate energies weighted by the Boltzmann distribution

$$U(T) = \frac{\sum_{\mu} \mathcal{H}(\mu) e^{-\frac{\mathcal{H}(\mu)}{k_B T}}}{Z(T)} = \frac{\sum_E E g(E) e^{-\frac{E}{k_B T}}}{Z(T)}, \quad (2.21)$$

represents the average energy of the system. Alternatively, the internal energy can be obtained by the differentiation of the free energy

$$U(T) = k_B T^2 \frac{\partial}{\partial T} \ln Z(T) \Big|_{N,V} = -T^2 \frac{\partial}{\partial T} \left( \frac{F}{T} \right) \Big|_{N,V}. \quad (2.22)$$

The amount of energy needed to increase the temperature of the system by one unit is given by the specific heat  $C_V$ , defined as a temperature derivative of the internal energy

$$C_V(T) = \left. \frac{\partial}{\partial T} U(T) \right|_{N,V} = -T \left. \frac{\partial^2}{\partial T^2} F(T) \right|_{N,V}. \quad (2.23)$$

On the other hand, starting with the third term in equation 2.21 we obtain the following expression

$$\begin{aligned} C_V(T) &= \frac{\partial}{\partial T} \frac{\sum_E E g(E) e^{-\frac{E}{k_B T}}}{Z(T)} = -\frac{1}{k_B T^2} \frac{\partial}{\partial \beta} \frac{\sum_E E g(E) e^{-\beta E}}{\sum_E g(E) e^{-\beta E}} \\ &= \frac{1}{k_B T^2} \left[ \left( \frac{\sum_E E^2 g(E) e^{-\beta E}}{Z(T)} \right) - \left( \frac{\sum_E E g(E) e^{-\beta E}}{Z(T)} \right)^2 \right] \\ &= \frac{1}{k_B T^2} (\langle E^2 \rangle - \langle E \rangle^2), \end{aligned} \quad (2.24)$$

where the last expression corresponds to the variance of the Boltzmann distribution. This result is of a profound physical importance, establishing the connection between the macroscopic response quantity  $C_V$ , and microscopic fluctuations.

### 2.2.1 Canonical analysis of phase transitions

Sudden dramatic changes of macroscopic properties, in response to small variations of an external control parameter, indicate that the system under investigation is undergoing a phase transition. Here we consider temperature-driven transitions and describe a classification scheme similar to Ehrenfest's.

In the thermodynamic limit, it is generally possible to identify some property of the system which is non-zero in the ordered phase and zero in the disordered phase, i.e. the order parameter [1, 9]. A standard example is the magnetization  $m$  in a ferromagnetic system, where  $m = 1$  in the ordered ferromagnetic phase and  $m = 0$  in the disordered

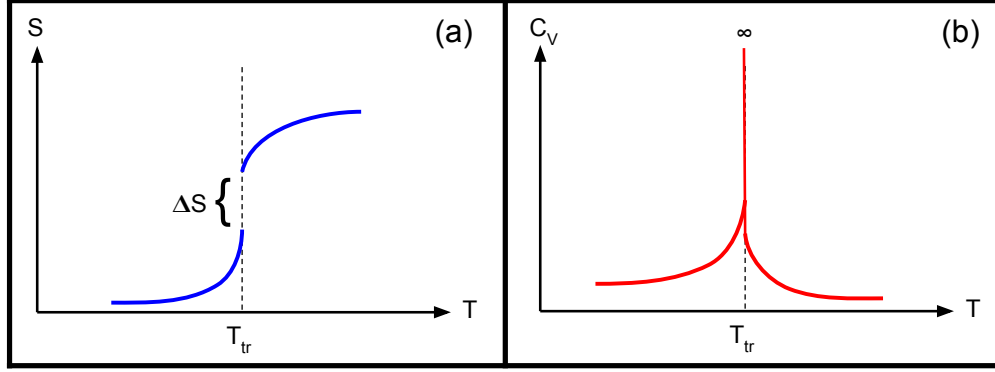


Figure 2.3: (a) The jump discontinuity in the canonical entropy  $S$ , (b) and the delta peak in the specific heat  $C_V$ , are characteristic of a first order phase transition.

paramagnetic phase. The derivative of the order parameter with respect to its conjugate variable defines a response quantity<sup>7</sup> which is discontinuous at the transition point. Order parameters also play a central role in the formulation of the Landau theory, where they serve as a basis for the expansion of the free energy around the transition point [10].

First order transitions are characterized by a jump discontinuity  $\Delta S$  in entropy and the coexistence of two distinct phases<sup>8</sup> at the transition temperature. The energetic separation between the two phases corresponds to the latent heat

$$\Delta Q = T_{\text{trans}} \Delta S, \quad (2.25)$$

where  $\Delta S$  is the height of the discontinuity and  $T_{\text{trans}}$  is the transition temperature. The specific heat  $C_V$  exhibits a delta peak at  $T_{\text{trans}}$ , as shown in Fig. 2.3 (b).

<sup>7</sup>In the case of the magnetization  $m$ , the appropriate conjugate thermodynamic variable is the external field  $H$ , and the corresponding response quantity is the magnetic susceptibility  $\chi$ .

<sup>8</sup>As a familiar example, consider the coexistence of gas bubbles and liquid at the boiling point of water.

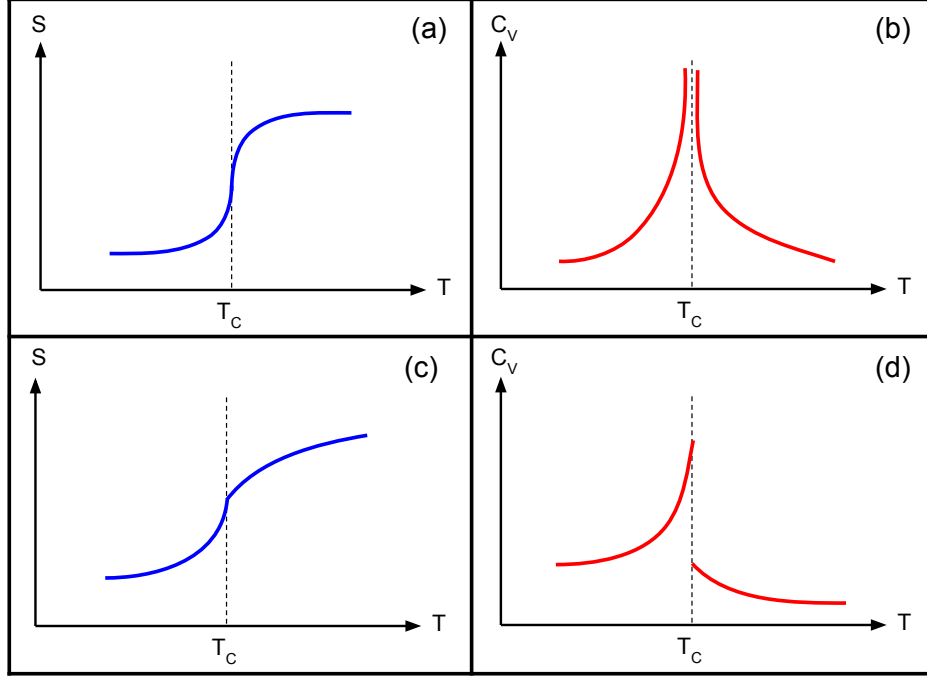


Figure 2.4: Second order transitions are characterized by discontinuities in response quantities, such as the specific heat. (a,b) In the case of a **critical** second order transition, the entropy  $S$  attains an infinite slope at  $T_c$  accompanied by a divergence in the specific heat  $C_V$ . (c,d) So called *lambda* transitions are characterized by a jump discontinuity in  $C_V$  and a cusp singularity in entropy.

Second order transitions do not possess discontinuities in entropy, and for that reason are often called *continuous* transitions. Instead, discontinuities are found in the second derivatives of the free energy with respect to temperature. It is customary to make use of equation 2.23, and consider the specific heat  $C_V$  which also contains the same discontinuities. In the vicinity of the transition point  $T_c$ , the specific heat exhibits a power law behavior  $C_V(\tau) \propto |\tau|^{-\alpha}$ , where  $\tau = (T - T_c)/T_c$  and  $\alpha$  is the associated critical exponent. Examples of common types of discontinuities of  $C_V$  are shown in Fig. 2.4. Other important quantities such as the magnetic susceptibility  $\chi$  and the correlation length  $\xi$  also exhibit a power law behavior near the transition point, governed by the critical exponents  $\gamma$  and  $\nu$  respectively.

The striking observation, that in the vicinity of the critical temperature  $T_c$ , the behavior of physical systems with diverse microscopic properties can be described in terms of the same critical exponents, is formalized in the theory of Universality [10].

### Canonical analysis in mesoscopic systems

The description of phase transitions in the terms of discontinuities and divergences is valid only in the thermodynamic limit. In situations where the thermodynamic behavior of a system is affected by finite size effects, this idealized description no longer applies. Nevertheless, the numerous examples of abrupt changes of macroscopic properties in finite systems necessitate the generalization of the theory. In order to avoid possible confusion, we shall refer to significant conformational changes in finite systems as *pseudophase transitions*. Similarly, sets of macrostates with sufficiently similar macroscopic properties will be denoted *pseudophases*.

In the generalized formalism, peaks in the specific heat and other response quantities indicate regions of increased thermodynamic activity, i.e. pseudophase transitions. The order of the transition is determined from the shape of the canonical energy distribution in the transition region. Bimodal distributions reveal the coexistence of two pseudophases and indicate a first-order transition [11]. The associated latent heat of the transition is given by the energetic separation between the two peaks in the distribution. Second-order transitions correspond to unimodal energy distributions. The power law behavior of response quantities contains significant finite-size corrections and in some cases is altogether not applicable [9]. An example of canonical analysis, applied to first- and second-order pseudophase transitions, is illustrated in Fig. 2.5.

It should be mentioned that second-order pseudophase transitions do not always produce peaks in the specific heat. In general, it is necessary to investigate the behavior of several response quantities in order to obtain an accurate picture of the transition properties of

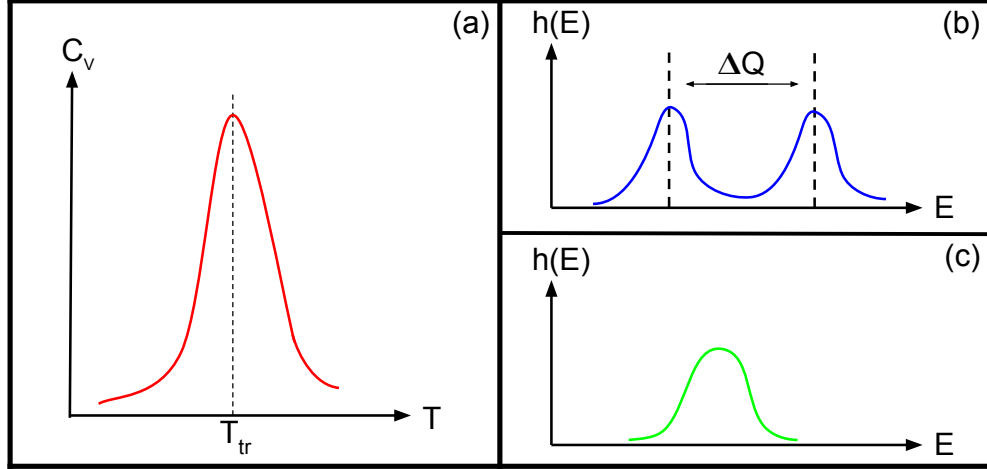


Figure 2.5: (a) The peak in the specific heat  $C_V$  indicates a region of heightened thermodynamic activity. (b) The two peaks in the bimodal canonical energy distribution correspond to the ordered and disordered pseudophases, energetically separated by the latent heat  $\Delta Q$ . Pseudophase coexistence and latent heat are reliable indicators of a first-order pseudophase transition. (c) Second-order transitions are marked by wide unimodal energy distributions at the transition point.

the system under investigation. However, due to finite size effects, the signals obtained from different quantities will in general not coincide at a single transition temperature. This reality further fortifies the argument that the microcanonical inflection-point analysis<sup>9</sup>, which defines a unique transition temperature in mesoscopic and macroscopic systems alike, is the preferred formalism for the analysis of finite systems.

---

<sup>9</sup>Introduced in Sec. 2.1.2

## 2.3 Alternative definitions of the density of states

In section 2.1 we have defined the microcanonical density of states  $g(E)$  as an integral over the surface of constant energy in the  $6N$ -dimensional phase space. We have argued that  $g(E)$  contains all the essential information about the thermodynamic properties of the system under consideration, and introduced the formalism of the microcanonical inflection-point analysis which uses the logarithm of  $g(E)$  as its starting point. In section 2.2 we have shown that the canonical partition function  $Z(T)$  can be obtained by performing a Laplace transform of  $g(E)$ . Clearly, the microcanonical density of states plays a fundamental role in equilibrium statistical mechanics, and as such needs to be carefully defined.

Two distinct definitions of the density of states arise from certain ambiguity in the exact meaning of the microcanonical ensemble in computational studies. The density of states can be defined in the context of the conformational microcanonical ensemble  $(N, V, E_p)$  as a function of the potential energy only

$$g_c(E_p) = \int \mathcal{D}\mathcal{Q} \, \delta(E_p - \mathcal{H}(\mathcal{Q})) \quad (2.26)$$

This definition is commonly used in Monte Carlo simulations of magnetic systems where the kinetic energy contributions have little physical significance and the sampling can be restricted to the conformational space. However, in systems where the transfer between potential and kinetic energy has important physical interpretation, the sampling of the full phase space becomes necessary. The standard definition of the microcanonical ensemble  $(N, V, E)$  is applied and the measured density of states becomes a function of the total system energy, which can be written as the sum of the potential and kinetic energies

$$E = E_p + E_k. \quad (2.27)$$



In order to distinguish between the two definitions, we shall use the symbol  $\Gamma(E)$  to represent the latter definition of the density of states. The connection between the conformational density of states and  $\Gamma(E)$  is expressed as a convolution [12]

$$\Gamma(E) = \int dE_k g_c(E - E_k) g_k(E_k), \quad (2.28)$$

where

$$g_k(E_k) = \int \mathcal{DP} \delta(E_k - \mathcal{H}(\mathcal{P})) \quad (2.29)$$

is the kinetic density of states obtained by integrating over the momentum space.

We shall now turn our attention to the consequence of choosing either the conformational or the full density of states as the starting point for a systematic analysis of the thermodynamic properties of a system under consideration. In the following we will discuss the impact of ignoring the momentum degrees of freedom on the results of both the canonical and microcanonical analysis. As an illustration, we will provide results from Monte Carlo simulations of two short flexible homopolymers.

### 2.3.1 Consequences for canonical analysis

The canonical partition function  $Z(T)$  and the microcanonical density of states are connected via a Laplace transform. We begin with the full density of states  $\Gamma(E)$  and using the definition from Eq. 2.28 write

$$Z(T) = \mathcal{L}\{\Gamma(E)\} = \mathcal{L}\{g_c * g_k\} = \mathcal{L}\{g_c\}\mathcal{L}\{g_k\}, \quad (2.30)$$

where the last step follows from the convolution theorem [13].

The partition function of the system can hence be conveniently written as a product of two independent partition functions

$$Z(T) = Z_c(T)Z_k(T), \quad (2.31)$$

which depend on the potential and kinetic energies respectively. It follows that the average ensemble energy can be expressed as the sum of the average potential and kinetic energies

$$\begin{aligned} U(T) &= k_B T^2 \frac{\partial}{\partial T} \ln Z \Big|_{N,V} \\ &= k_B T^2 \frac{\partial}{\partial T} \ln Z_c \Big|_{N,V} + k_B T^2 \frac{\partial}{\partial T} \ln Z_k \Big|_{N,V} \\ &= \langle E_c \rangle + \langle E_k \rangle. \end{aligned} \quad (2.32)$$

With the exception of systems with rigid constraints, the average kinetic energy is given by the equipartition theorem

$$\langle E_k \rangle = \frac{3Nk_B T}{2}, \quad (2.33)$$

where  $N$  is the number of particles in the system. It follows that the specific heat  $C_V$  obtains only a trivial additive constant from the kinetic energy term

$$\begin{aligned} C_V(T) &= \frac{\partial}{\partial T} U(T) \Big|_{N,V} \\ &= \frac{\partial}{\partial T} \langle E_c \rangle \Big|_{N,V} + \frac{\partial}{\partial T} \frac{3Nk_B T}{2} \\ &= C_{V,\text{conf.}} + \frac{3Nk_B}{2}. \end{aligned} \quad (2.34)$$

In conclusion, the locations and shapes of signals for pseudophase transitions are not affected by the inclusion of the momentum space into a sampling scheme. To substantiate this assertion, in Fig. 2.6 we present the results from a Monte Carlo study of a short

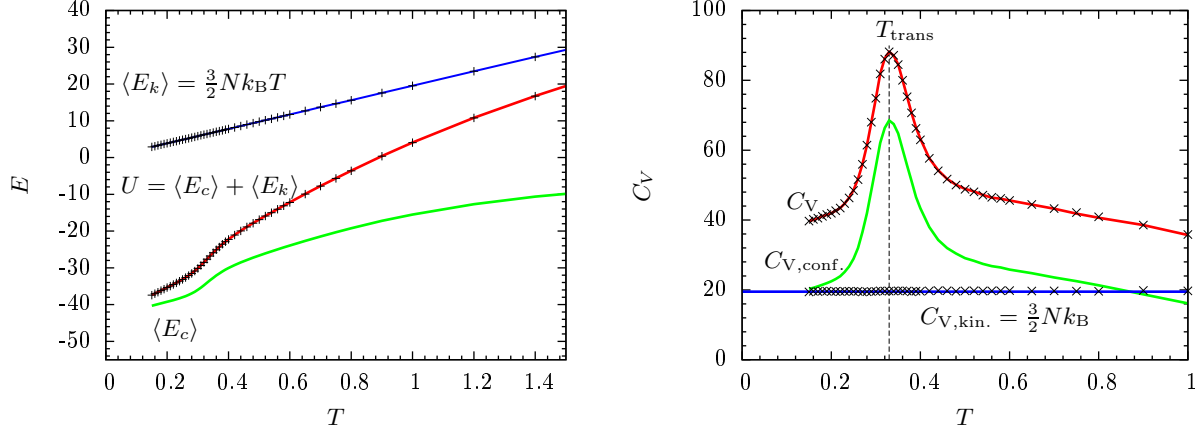


Figure 2.6: Results of a Monte Carlo simulation of a short flexible homopolymer of length  $N = 13$ . The average kinetic energy  $\langle E_k \rangle$  and the kinetic contributions  $C_{V,\text{kin.}}$  towards the specific heat are plotted as points on top of their respective theoretical curves (blue). The average potential energy  $\langle E_c \rangle$  and the configurational specific heat  $C_{V,\text{conf.}}$  (green) were obtained by sampling of the configurational space. Sampling of the full phase space was performed to obtain the total average energy  $U$  and the combined specific heat  $C_V$  (red). As expected, the combined specific heat is identical to  $C_{V,\text{conf.}}$ , except for a trivial additive constant.

flexible homopolymer. The average kinetic energy  $\langle E_k \rangle$  and the kinetic contributions  $C_{V,\text{kin.}}$  towards the specific heat are plotted as points on top of their respective theoretical curves (blue), showing good agreement with the predicted values. The average potential energy  $\langle E_c \rangle$  and the configurational specific heat  $C_{V,\text{conf.}}$  (green) were obtained by the sampling of the configurational space only. Sampling of the full phase space was performed to obtain the total average energy  $U$  and the combined specific heat  $C_V$  (red). As expected, the combined specific heat is identical to  $C_{V,\text{conf.}}$ , except for a trivial additive constant. The estimate of the transition temperature is independent of the choice of either definition of the density of states.

### 2.3.2 Consequences for microcanonical analysis

The application of the Laplace transform to the total density of states  $\Gamma(E)$ , allowed us to conveniently disentangle the convolution in Eq. 2.28 into separate kinetic and conformational contributions [Eq. 2.30]. Unfortunately, in the microcanonical ensemble no such simplification is readily available. Let us however consider a class of physical systems whose momenta and positional degrees of freedom are independent. Explicit integration over the momentum space yields a simple expression for the kinetic density of states

$$g_k(E_k) = \int \mathcal{DP} \delta(E_k - \mathcal{H}(\mathcal{P})) = E_k^{\frac{3N-2}{2}}. \quad (2.35)$$

Combining the result with Eq. 2.28 we obtain

$$\Gamma(E) = \int dE_k g_c(E - E_k) E_k^{\frac{3N-2}{2}}. \quad (2.36)$$

Next, taking a derivative with respect to the total energy  $E$  and dividing both sides by  $\Gamma(E)$  we get two equivalent expressions for the microcanonical inverse temperature

$$\beta(E) = \int dE_k \frac{3N-2}{2E_k} \left[ \frac{g_c(E - E_k) E_k^{\frac{3N-2}{2}}}{\Gamma(E)} \right] \quad (2.37)$$

$$= \int dE_p \beta_c(E_p) \left[ \frac{g_c(E_p) (E - E_p)^{\frac{3N-2}{2}}}{\Gamma(E)} \right]. \quad (2.38)$$

Recognizing the two terms enclosed in square brackets as the microcanonical probability densities for the kinetic and potential energies, we can rewrite equations 2.37 and 2.38 as

$$\beta(E) = \int dE_k \frac{3N-2}{2E_k} \rho(E_k)_E = \frac{3N-2}{2} \left\langle \frac{1}{E_k} \right\rangle, \quad (2.39)$$

and

$$\beta(E) = \int dE_p \beta_c(E_p) \rho(E_p)_E = \langle \beta_c \rangle. \quad (2.40)$$

The microcanonical inverse temperature, obtained by the differentiation of the total density of states, can therefore be interpreted as an average of the conformational and kinetic analogs weighted by their respective microcanonical probability distributions.

When the number of particles in the system is large, the probability densities  $\rho(E_k)_E$  and  $\rho(E_p)_E$  are expected to be sharply peaked around the most probable kinetic  $\bar{E}_k$  and potential  $\bar{E}_p$  energies respectively. We can therefore apply the saddle point approximation to the integrals in equations [2.39, 2.40] and obtain the following first order approximations for the inverse temperature

$$\beta(E) \approx \beta_c(\bar{E}_p), \quad (2.41)$$

and

$$\beta(E) \approx \frac{3N-2}{2} \left( \frac{1}{\bar{E}_k} \right). \quad (2.42)$$

The first expression suggests that it is possible to reconstruct  $\beta(E)$  from the conformational inverse temperature  $\beta_c$ , and that the two quantities contain essentially the same information. We test the validity of this hypothesis by comparing the microcanonical results of Monte Carlo simulations of a flexible elastic 55-mer, which were carried out in both the conformational space and the full phase space.

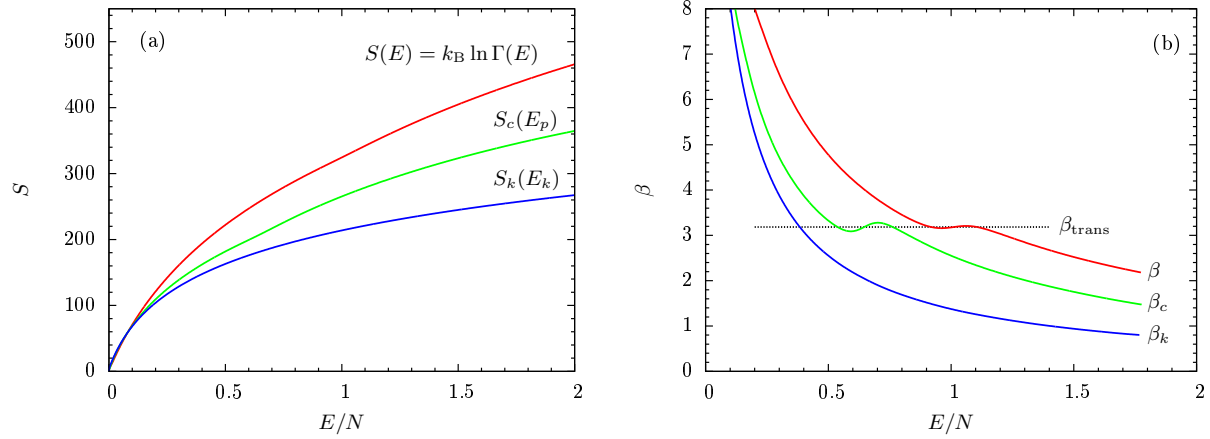


Figure 2.7: Comparison of microcanonical results from a Monte Carlo simulation of a flexible homopolymer of length  $N = 55$ . (a) The combined  $S$ , conformational  $S_c$ , and kinetic  $S_k$  entropy curves. (b) The kinetic inverse temperature  $\beta_k$  is a strictly convex function and the application of the inflection-point analysis reveals no transition signals. The conformational inverse temperature  $\beta_c$  clearly differs from  $\beta(E)$ , however both indicate a first-order pseudophase transition at virtually the same temperature.

The kinetic entropy in Fig. 2.7 is a strictly concave function and the application of the inflection-point analysis to the corresponding inverse temperature  $\beta_k$  reveals no transition signals. The conformational inverse temperature clearly differs from  $\beta(E)$ , however both indicate a first-order pseudophase transition at virtually the same temperature. In Fig. 2.8 we show the comparison between the true  $\beta(E)$  and the reconstruction obtained from the conformational inverse temperature according to equations 2.41 and 2.42. It is evident that the approximation is valid, except in the back-bending region of the first-order transition due to the bimodality of the probability densities  $\rho(E_k)_E$  and  $\rho(E_p)_E$ .

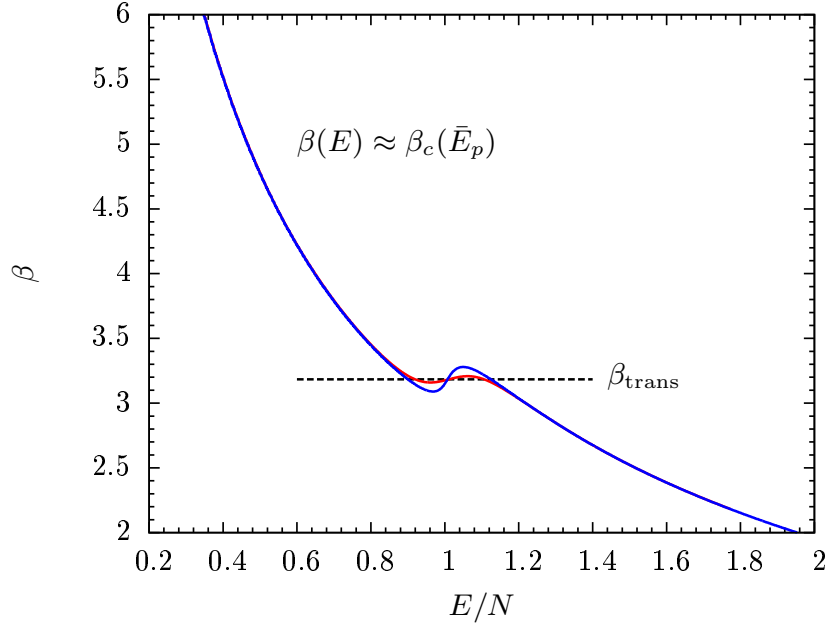


Figure 2.8: Comparison of the inverse microcanonical temperature  $\beta(E)$  (red) and the conformational inverse temperature  $\beta_c(\bar{E}_p)$  (blue) evaluated at the most probable potential energy  $\bar{E}_p$ . The approximation introduced in equation 2.41 holds except in the back-bending region of the first-order pseudophase transition. The inverse transition temperature  $\beta_{\text{trans}}$  obtained from the two quantities is virtually identical.

The expression in equation 2.42 can be rewritten as

$$k_{\text{B}}T(E) \approx \frac{2}{3N-2} \left( \frac{1}{\bar{E}_k} \right)^{-1}, \quad (2.43)$$

which clearly resembles the well known relationship between the canonical temperature and the average kinetic energy. In the thermodynamic limit, this approximation becomes exact and the equivalency of the microcanonical and canonical ensembles is restored.

# Chapter 3

## Computational Methods

Computational algorithms are powerful tools that enable the investigation of many-body physical systems under thermal conditions, that are far too complex to be solved analytically. In fact, only a handful of systems with large number of degrees of freedom are exactly solvable<sup>1</sup>, and even the simplest solutions often require bewildering mathematical gymnastics. Consequently, computational studies are the main source of advances in the fundamental understanding of complex microscopic and mesoscopic systems such as biopolymers and proteins [1].

Two complementary classes of computational algorithms have been particularly successful in unravelling the thermodynamic properties of physical systems. *Molecular dynamics* simulations generate a single phase space trajectory by updating the positions and momenta of every particle in a system according to Hamilton's equations [14, 15]. Alternatively, carrying out a stochastic sampling of the phase space, *Monte Carlo* simulations estimate the equilibrium properties without an explicit consideration of the system's dynamics [1, 9]. In this chapter, we shall focus our attention to Markov chain Monte Carlo methods. We will briefly discuss the essential theory and introduce the well established Metropolis and Paral-

---

<sup>1</sup>The most prominent examples of exactly solvable systems with large number of degrees of freedom are the ideal gas and the two dimensional Ising model.



lel Tempering algorithms as well as the lesser known Multiple Gaussian modified ensemble method.

### 3.1 Markov chain Monte Carlo

The aim of all Monte Carlo methods is to extract the equilibrium thermodynamic properties of physical systems by performing an efficient stochastic sampling of the phase space. For this purpose, a set of random microstates  $\{\mu_1, \mu_2, \dots, \mu_M\}$  is generated according to some previously known probability distribution  $p(\mu_i)$ , and the expectation value for any observable  $O(\mu)$  is estimated by calculating the average

$$\bar{O} = \frac{1}{M} \sum_{i=1}^M O(\mu_i). \quad (3.1)$$

In most Monte Carlo methods, the set of random microstates is generated according to a discrete-time Markov chain (DTMC) [16]. Markov chains are sequences of random states, generated according to the time-independent transition probabilities  $T(\mu \rightarrow \nu)$  which satisfy the Markov property. In simple terms, the probability of moving to state  $\nu$  from state  $\mu$  depends only on the present state, and is independent of the history of the process. In order to achieve the correct statistical sampling of an equilibrium thermodynamic ensemble, the following conditions must also be satisfied.

The process must be **ergodic**, i.e., there must be a path of non-zero probability between any pair of states. More formally, the state space  $\mathcal{S}$  of the Markov chain must consist of a single aperiodic recurrence class. When ergodicity is satisfied, the ensemble average  $\langle O \rangle$  can be approximated by the measured expectation value  $\bar{O}$  [Eq. 3.1]

$$\bar{O} = \frac{1}{M} \sum_{i=1}^M O(\mu_i) \approx \langle O \rangle = \int \mathcal{D}\mathcal{P} \mathcal{D}\mathcal{Q} O(\mathcal{P}, \mathcal{Q}) p(\mathcal{P}, \mathcal{Q}), \quad (3.2)$$

where  $M$  is the length of the Markov chain. According to the ergodic hypothesis [15], the approximation becomes exact in the limit of an infinitely long Markov chain

$$\lim_{M \rightarrow \infty} \frac{1}{M} \sum_{i=1}^M O(\mu_i) = \int \mathcal{D}\mathcal{P} \mathcal{D}\mathcal{Q} O(\mathcal{P}, \mathcal{Q}) p(\mathcal{P}, \mathcal{Q}). \quad (3.3)$$

The time evolution of a discrete-time Markov process is described by the master equation

$$\frac{\Delta p(\mu)}{\Delta t} = \sum_{\nu} p(\nu) T(\nu \rightarrow \mu) - p(\mu) T(\mu \rightarrow \nu). \quad (3.4)$$

The equilibrium condition requires that the probability distribution  $p(\mu)$  is stationary. In other words, the probability currents into and out of the state  $\mu$  must be always equal

$$\sum_{\nu} p(\nu) T(\nu \rightarrow \mu) = \sum_{\nu} p(\mu) T(\mu \rightarrow \nu). \quad (3.5)$$

Also known as the **balance** condition, equation 3.5 sometimes allows for solutions that are not permitted in the equilibrium ensemble [9]. The stricter condition of **detailed balance** requires that the probability of a transfer between any two states must be equal to the probability of the reverse process. Embodied in the expression

$$p(\mu) T(\mu \rightarrow \nu) = p(\nu) T(\nu \rightarrow \mu), \quad (3.6)$$

this condition is sufficient to prevent any non-physical solutions as well as to ensure that the process is invariant under time reversal.

Having introduced the conditions of ergodicity and detailed balance, we can now derive the expression for transition probabilities which will ensure correct stochastic sampling according to an equilibrium distribution  $p(\mu)$ . For convenience, we will separate the transition probabilities into two separate terms and write

$$T(\mu \rightarrow \nu) = s(\mu \rightarrow \nu) a(\mu \rightarrow \nu). \quad (3.7)$$

Assuming the current state  $\mu$ , the probability of generating a new state  $\nu$  is given by the selection probability  $s(\mu \rightarrow \nu)$ , while the probability of accepting the proposed update is controlled by the *acceptance* probability  $a(\mu \rightarrow \nu)$ . Combining equations 3.6 and 3.7, we express the ratio of the transition probabilities as

$$\frac{T(\mu \rightarrow \nu)}{T(\nu \rightarrow \mu)} = \frac{s(\mu \rightarrow \nu) a(\mu \rightarrow \nu)}{s(\nu \rightarrow \mu) a(\nu \rightarrow \mu)} = \frac{p(\nu)}{p(\mu)}. \quad (3.8)$$

The ratio of the forward and backward selection probabilities  $\sigma(\mu, \nu) = s(\mu \rightarrow \nu) / s(\nu \rightarrow \mu)$  depends on the choice of the particular update scheme. In the remainder of this thesis, we shall assume that the forward and backward selection probabilities are equal and the ratio equals to unity, which is valid for most local Monte Carlo updates. This simplifying assumption allows us to rewrite equation 3.8 without making explicit references to the selection probabilities

$$\frac{a(\mu \rightarrow \nu)}{a(\nu \rightarrow \mu)} = \frac{p(\nu)}{p(\mu)}. \quad (3.9)$$

### 3.1.1 Metropolis sampling

Any set of acceptance probabilities which satisfies equation 3.9 is allowable, however the standard choice is to set the higher of the two probabilities to unity. This yields the well known Metropolis acceptance criterion [9, 17]:

$$a(\mu \rightarrow \nu) = \min \left( 1, \frac{p(\nu)}{p(\mu)} \right). \quad (3.10)$$

Under most circumstances, Metropolis sampling is carried out according to the canonical microstate probability distribution  $p(\mu) \propto e^{-\beta E(\mu)}$ , where  $\beta$  is the inverse canonical temper-

ature. Hence the acceptance probability is governed by the energy difference between the proposed and the current states

$$a(\mu \rightarrow \nu) = \min \left( 1, \frac{e^{-\beta E(\nu)}}{e^{-\beta E(\mu)}} \right) = \min(1, e^{-\beta \Delta E}). \quad (3.11)$$

The average of the observable  $O(\mu)$ , measured over the length of a finite Metropolis run, serves as an estimate for the canonical expectation value  $\langle O \rangle$  [Eq. 3.2]. In the limit of an infinite run, this approximation becomes exact [Eq. 3.3]. However, since all simulations are of finite length, it is imperative to account for the statistical errors introduced due to the finiteness of the measured data sets. The standard bias corrected error estimator for the calculated average  $\bar{O}$ , obtained from a finite set of  $M$  uncorrelated measurements, is written as

$$\text{err}(\bar{O}) = \pm \sqrt{\frac{1}{M(M-1)} \sum_m (O_m - \bar{O})^2}. \quad (3.12)$$

In reality, most measurements obtained from Monte Carlo simulations are correlated. Hence it is necessary to introduce the modified error estimator

$$\text{err}(\bar{O}) = \pm \sqrt{\frac{1}{M(M_{\text{eff}} - 1)} \sum_m (O_m - \bar{O})^2}, \quad (3.13)$$

where  $M_{\text{eff}}$  is the number of uncorrelated measurements<sup>2</sup>.

The Metropolis method provides the means for an efficient sampling of microstates which are dominant at a given temperature. However, the microstates which are found in the tails of the canonical energy distribution are rarely visited. Further shortcomings of the Metropolis algorithm, such as the propensity for getting trapped in low-energy configurations and the notorious reduction in sampling efficiency near pseudophase transitions, motivate the introduction of more efficient sampling methods.

---

<sup>2</sup>For detailed description of the more practical *binning* and *jackknife* error estimation methods, please refer to chapter 4 in [1].

### 3.1.2 Parallel tempering

In situations where the Metropolis method fails to produce data of reasonable quality, the standard way of increasing sampling efficiency is to perform the simulation in a conveniently chosen *generalized ensemble*<sup>3</sup>. In parallel tempering [18–21], multiple canonical ensembles with different inverse temperatures  $\{\beta_1 < \beta_2 < \dots < \beta_N\}$  are simulated in parallel according to the standard Metropolis scheme. In this context, the generalized ensemble is defined as the direct product of  $N$  canonical ensembles, and the partition function is given by

$$Z_{\text{PT}}(\beta_1, \beta_2, \dots, \beta_N) = \prod_{i=1}^N Z_{\text{can}}(\beta_i). \quad (3.14)$$

At judiciously chosen intervals, an exchange of conformations between adjacent temperature threads  $i$  and  $j$  is proposed. The combined probability for states  $(\mu, \nu)$  at respective temperatures  $(\beta_i, \beta_j)$  is given by

$$p_{\mu\nu} = \frac{e^{-\beta_i E(\mu)}}{Z_{\text{can}}(\beta_i)} \frac{e^{-\beta_j E(\nu)}}{Z_{\text{can}}(\beta_j)}, \quad (3.15)$$

and the acceptance probability for the exchange of conformations is obtained from Eq. 3.10

$$\begin{aligned} a(\mu \leftrightarrow \nu; \beta_i, \beta_j) &= \min \left( 1, \frac{e^{-\beta_i E(\nu)} e^{-\beta_j E(\mu)}}{e^{-\beta_i E(\mu)} e^{-\beta_j E(\nu)}} \right) \\ &= \min \left( 1, e^{[\beta_j - \beta_i][E(\nu) - E(\mu)]} \right). \end{aligned} \quad (3.16)$$

The exchange rates are governed by the overlap of canonical energy distributions of the adjacent ensembles, hence the efficiency of the method depends sensitively on the choice of an appropriate temperature set. As a general rule, the density of temperatures must be increased in ordered phases and in the vicinity of pseudophase transitions.

---

<sup>3</sup>The microstate probability distribution of a generalized ensemble can be arbitrary and does not have to bear any resemblance to the Boltzmann distribution.

In principle, each replica is allowed to traverse the entire simulated temperature range which leads to the decrease of the autocorrelation time and reduces the likelihood of getting trapped in local energy minima at low temperatures. However, the performance of this method rapidly decreases near first-order transitions, where the joint effects of the entropic suppression of intermediate states and the energetic separation between the ordered and disordered pseudophases, virtually prevent the exchange of configurations between adjacent ensembles.

### 3.1.3 Multiple Gaussian modified ensemble

An alternative generalized ensemble method that offers improved performance is based on the combination of parallel tempering with the Gaussian modified ensemble (GME) method [22]. The idea behind GME is to modify the canonical Boltzmann distribution by multiplying it by a Gaussian function, in order to promote sampling in selected energy regions. The mean energy  $E_G$  and the variance  $\Delta E_G^2$  of the Gaussian form controls the location and the width of the region of enhanced sampling. The modified microstate probability at the inverse temperature  $\beta$  is given by

$$P_{\text{GME}}(\mu) \propto e^{-\beta E_\mu - (E_\mu - E_G)^2 / \Delta E_G^2}. \quad (3.17)$$

The measurements obtained from simulations in a modified ensemble must be reweighted in order to obtain the expectation values in the original canonical ensemble. In the context of the modified Gaussian ensemble this is done by calculating

$$\langle O \rangle_{\text{can}, \beta} = \frac{\sum_{i=1}^M O_i e^{\beta(E_i - E_G)^2 / \Delta E_G^2}}{\sum_{i=1}^M e^{\beta(E_i - E_G)^2 / \Delta E_G^2}}. \quad (3.18)$$

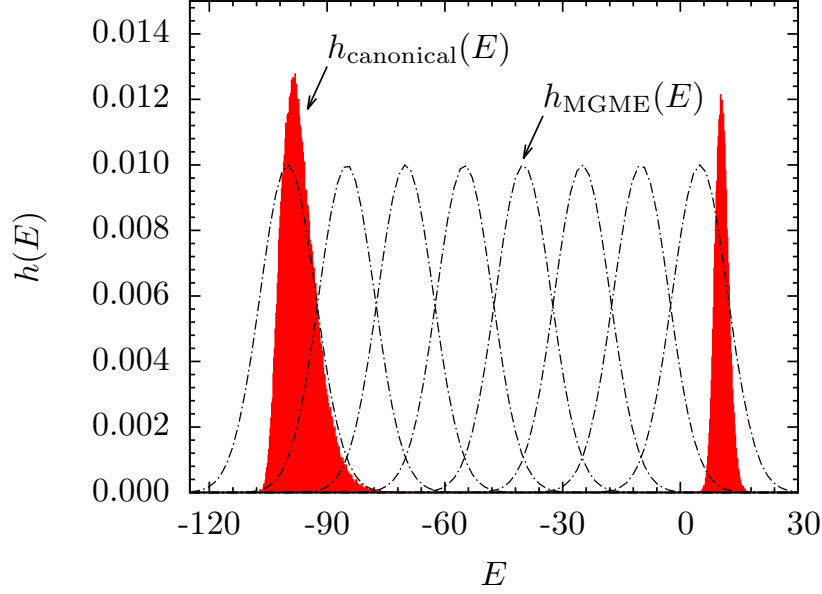


Figure 3.1: Canonical and GME energy histograms at a first-order pseudophase transition. The bimodal canonical energy histogram indicates the coexistence of ordered and disordered pseudophases, separated by an entropically suppressed energy region. Each GME ensemble enhances the sampling of suppressed states over a limited energy range.

Strong first-order transitions with bimodal energy distributions typically require several overlapping GME ensembles to cover the relevant energy range, as illustrated in Fig. 3.1. The acceptance probability for the exchange of conformations  $(\mu, \nu)$  between neighboring GME ensembles with mean energies  $(E_{G,i}, E_{G,j})$  at a constant inverse temperature  $\beta$  is

$$a(\mu \leftrightarrow \nu) = \min(1, e^{\Delta G}), \quad (3.19)$$

where

$$\Delta G = \frac{(E_\mu - E_{G,j})^2 - (E_\nu - E_{G,j})^2}{\Delta E_{G,j}^2} - \frac{(E_\nu - E_{G,i})^2 - (E_\mu - E_{G,i})^2}{\Delta E_{G,i}^2}. \quad (3.20)$$

The direct product of GME ensembles defines the multiple Gaussian modified ensemble (MGME). With a proper choice of ensemble parameters  $(E_G, \Delta E_G)$  it is possible to achieve a significantly enhanced sampling of previously inaccessible states. This can be further improved by allowing for exchanges between GME ensembles at different temperatures. However, previous knowledge of the system under consideration is usually needed to make a reasonable estimate for the ensemble parameters. Therefore other more systematic methods, such as the multicanonical [23–28] and Wang-Landau sampling [29–31], are often used.

## 3.2 Histogram reweighting methods

In chapter 2, we have introduced the microcanonical inflection point analysis as the means for the systematic study of pseudophase transitions in the microcanonical ensemble. Application of this method however presumes the precise knowledge of the microcanonical density of states  $g(E)$  [Eq 2.3]. Previously introduced sampling methods do not directly measure  $g(E)$  but rather generate canonical energy histograms  $h(E, \beta_i)$ . Hence, it is necessary to introduce a general method for estimating the density of states from energy histograms.

### 3.2.1 Multiple-histogram reweighting

Canonical histogram  $h(E, \beta_i)$  provides an approximation for the Boltzmann distribution  $p_{\text{can}}(E, \beta_i)$ , which is itself proportional to the microcanonical density of states

$$h(E, \beta_i) \approx p_{\text{can}}(E, \beta_i) \propto g(E) e^{-\beta_i E} \quad (3.21)$$

Therefore each histogram yields an estimate of the density of states

$$\bar{g}_i(E) = h(E, \beta_i) e^{\beta_i E} \quad (3.22)$$



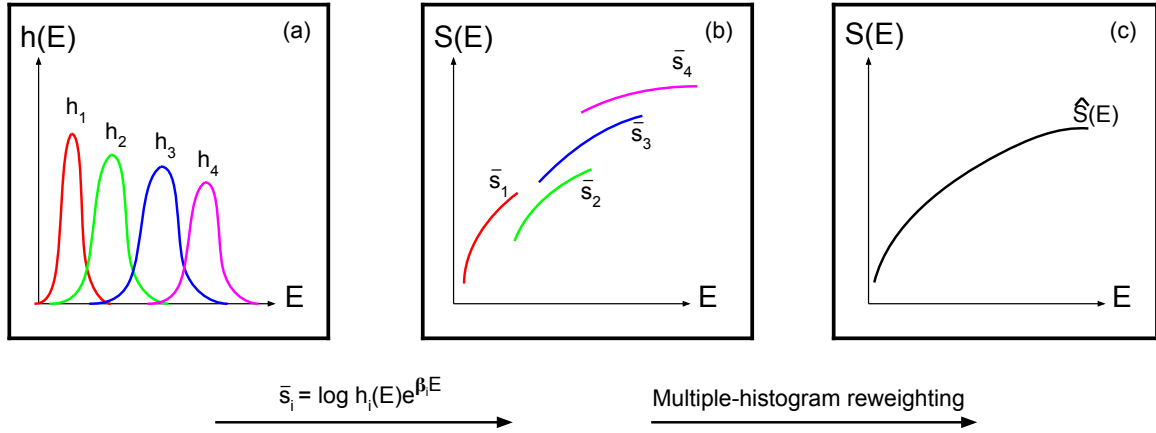


Figure 3.2: (a) Illustration of the canonical energy histograms  $h(E, \beta_i)$ , (b) the individual estimates of the logarithm of the density of states  $\bar{S}_i(E)$ , (c) and the combined estimate of the logarithm of the density of states  $\hat{S}(E)$  obtained by reweighting.

Individual estimates  $\bar{g}_i(E)$  are only reliable for energies in the vicinity of the peak of the canonical histogram obtained at the temperature  $\beta_i$ . Therefore a sufficient overlap between the histograms of adjacent replicas is necessary to ensure that an accurate estimate of the density of states can be obtained for the entire energetic range.

The task is now to combine the individual estimates  $\bar{g}_i(E)$  and obtain an improved estimate  $\hat{g}(E)$ . Unfortunately, general Monte Carlo methods do not yield absolute estimates for the partition function  $Z(\beta)$  and the estimates  $\bar{g}_i(E)$  cannot be directly related if obtained at different temperatures. However, it is possible to introduce a reference partition function

$$\hat{Z}_i = \sum_E \hat{g}(E) e^{-\beta_i E}, \quad (3.23)$$

which serves as the appropriate weight in the estimator for the density of states

$$\hat{g}(E) = \frac{\sum_{i=1}^R h(E, \beta_i)}{\sum_{i=1}^R M_i \hat{Z}_i^{-1} e^{-\beta_i E}}. \quad (3.24)$$

The equations 3.23 and 3.24 must be solved iteratively until  $\hat{g}(E)$  has converged. The relationship between the energy histograms, the individual estimates  $\bar{g}_i(E)$ , and the final estimate  $\hat{g}(E)$  of the density of states is illustrated in Fig. 3.2. For detailed derivation and a further discussion of the multiple-histogram reweighting method please refer to [32, 33].

### 3.2.2 Beziere smoothing

The estimator for the density of states, obtained either by multiple-histogram reweighting or directly by multicanonical sampling, is not a smooth function but rather a discrete set of stochastic values. The formalism of the microcanonical inflection point analysis requires the accurate knowledge of its energy derivatives. These have to be computed by numerical differentiation which is prone to enhancing the random statistical fluctuations of the original data set. It is therefore desirable to approximate the density of states by a smooth analytic function, which can be done very effectively with Beziér curves [1, 34].

Beziér curve of order  $n$  is a parametric curve defined by a set of  $(n + 1)$  control points  $\{P_0, P_1, \dots, P_n\}$  and the formula

$$B(t) = \sum_{i=0}^n \mathcal{B}_i^{(n)}(t) P_i, \quad (3.25)$$

where  $B_i^{(n)}$  are the Bernstein basis polynomials [35] of degree  $n$

$$B_i^{(n)}(t) = \binom{n}{i} (1-t)^{n-i} t^i. \quad (3.26)$$

The discrete values of the estimated density of states  $g(E_i)$  serve as control points for the approximating Beziér curve. Assuming that the set of  $(n + 1)$  control points  $\{g(E_0), g(E_1), \dots, g(E_n)\}$  is equally spaced in the energy space over the interval  $[E_{\min}, E_{\max}]$ ,

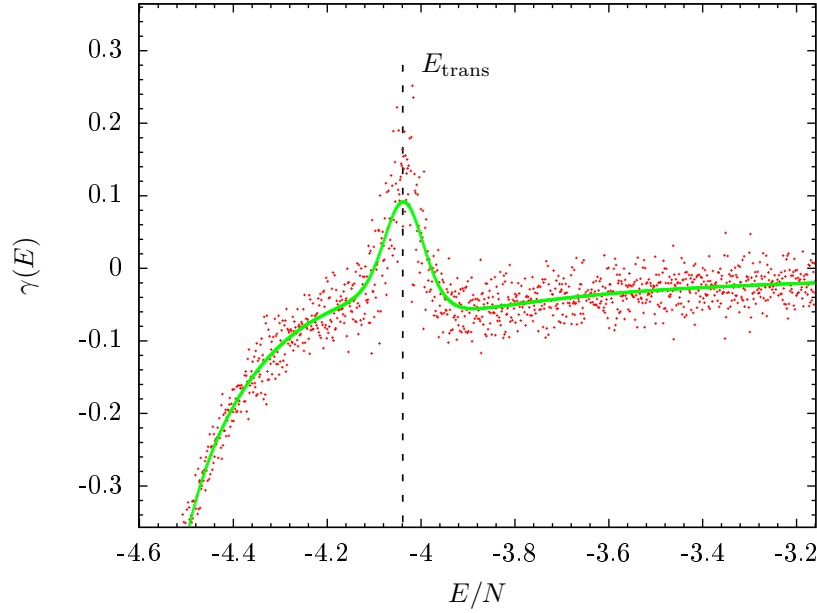


Figure 3.3: Comparison between the noisy derivative of the microcanonical inverse temperature  $\gamma(E) = d\beta/dE$  and the Beziér approximation  $\gamma_{\text{bez}}(E)$ . The systematic error in the Beziér approximation is visible near  $E_{\text{trans}}$ , where the curvature of  $\gamma(E)$  changes abruptly.

the approximating Beziér function can be directly calculated from

$$g_{\text{bez}}(E) = \sum_{i=0}^n \binom{n}{i} \left( \frac{E_{\text{max}} - E}{E_{\text{max}} - E_{\text{min}}} \right)^{n-i} \left( \frac{E - E_{\text{min}}}{E_{\text{max}} - E_{\text{min}}} \right)^i g(E_i). \quad (3.27)$$

The numerical error introduced by the approximation scheme is typically much smaller than the random statistical fluctuations in the original noisy data set [1]. However it should be mentioned that Beziér smoothing may introduce systematic errors to the derivatives of  $g(E)$  in areas of abrupt changes in curvature. This is illustrated in Fig. 3.3 where we compare the noisy derivative of the microcanonical inverse temperature  $\gamma(E) = d\beta/dE$  and the Beziér approximation  $\gamma_{\text{bez}}(E)$  in the region of a first-order pseudophase transition.

### 3.3 Simple Monte Carlo updates

The efficiency of Monte Carlo simulations depends in equal measure on the choice of the sampling algorithm and on the selection of appropriate conformational updates. All update sets must be ergodic, i.e., it must be in principle possible to connect any two arbitrary states through a finite number of updates. Additionally, all updates must preserve the constraints of the model, such as volume exclusion and boundary conditions. The efficiency of individual updates depends strongly on the model to which they are being applied. Hence, there is no general set of updates that guarantees good performance across different physical models. In the following, we shall briefly discuss conformational updates which are suitable for simulations of off-lattice polymers and proteins.

#### 3.3.1 Single displacement update

The single displacement update is easy to implement, satisfies ergodicity, and has equal forward and backward selection probabilities. The original conformation of a polymer chain  $\mathbf{R} = \{\mathbf{r}_1, \mathbf{r}_2, \dots, \mathbf{r}_N\}$  is updated by a random<sup>4</sup> displacement  $\Delta\mathbf{r}_i$  of a randomly selected  $i$ -th monomer. The displacement vector is defined in the Cartesian coordinates as  $\Delta\mathbf{r}_i = (\Delta x_i, \Delta y_i, \Delta z_i)$ , where each component is selected with uniform probability from some interval  $[-l, l]$ . In general, longer displacement updates lead to larger energy differences between the old and the new states  $\Delta E = E_{\text{new}} - E_{\text{old}}$ . In Monte Carlo simulations, large positive values of the ratio  $\Delta E/T$  result in an exponential suppression of the acceptance rates [Eq. 3.11]. In order to achieve acceptance rates within the optimal range of  $\sim 30\% - 70\%$ , the set of temperature dependent displacement parameters  $l(T_i)$  must be determined. Unfortunately, for most off-lattice polymer models, only very short displace-

---

<sup>4</sup>Monte Carlo simulations make extensive use of pseudo-random numbers. The popular Mersenne Twister pseudo-random number generator [36] is used throughout this thesis. For more information on the ‘art’ of random number generation please refer to [9].

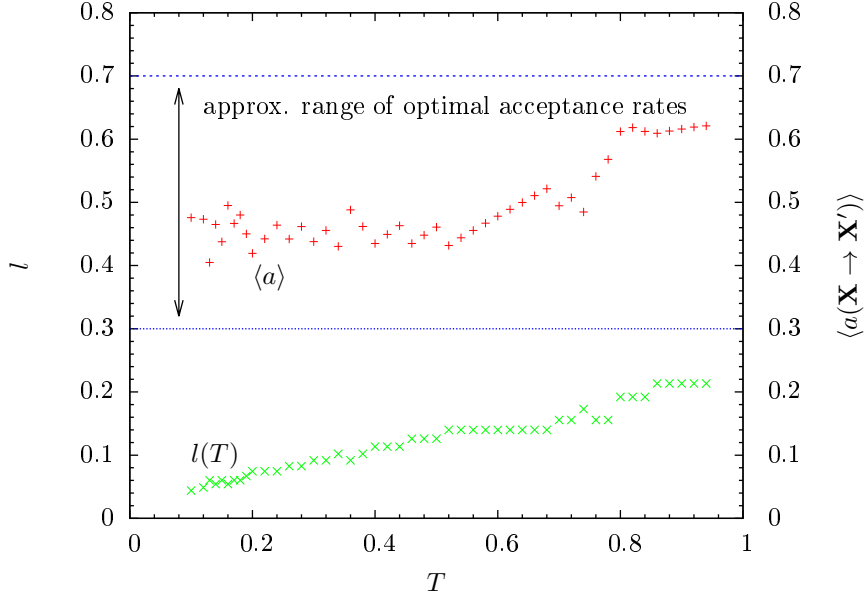


Figure 3.4: Example of a distribution of the temperature dependent displacement parameter  $l(T)$ , used in a parallel tempering simulation of a flexible elastic 55-mer. The values of  $l(T)$  were selected to keep the average acceptance rates  $\langle a \rangle$  within the optimal range of  $\sim 30\% - 70\%$ .

ment updates are allowed at low temperatures and the generated sequence of states becomes strongly correlated. An example of the temperature dependence of  $l(T_i)$ , obtained from a simulation of a flexible elastic 55-mer, is shown in Fig. 3.4. Polymer models which contain stiff bonds cannot be sampled using displacement updates and require more sophisticated rotational updates [1].

### 3.3.2 Pivot update

The pivot update consists of rotating a portion of the polymer chain over a randomly chosen rotation axis. This allows for a global change in the polymer conformation and decreases the correlation between the sampled states. In practice, first a random monomer is selected to serve as the pivot and the direction of the rotation axis is defined by a random vector

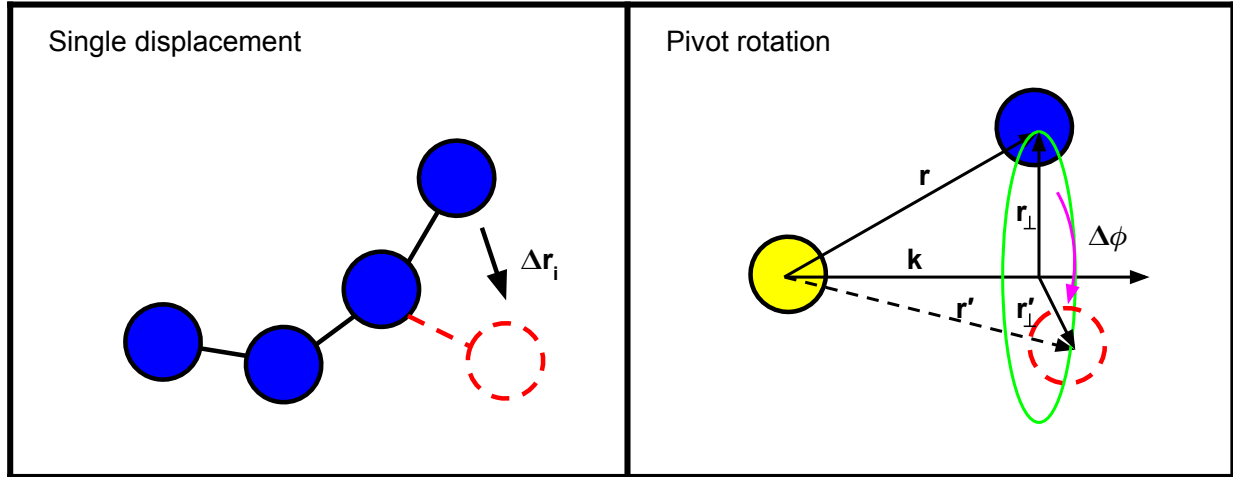


Figure 3.5: Schematic depiction of the single-displacement and the rotational pivot updates. In a displacement update, a randomly selected monomer is moved according to a randomly generated displacement vector  $\Delta \mathbf{r}_i$ . The pivot update consists of rotating a portion of the polymer chain over a randomly chosen axis  $\mathbf{k}$  by a random angle  $\Delta \phi$ .

**k.** With equal probability, either terminus of the chain is selected for rotation. The vector which connects the pivot to any monomer which is to be rotated is denoted as  $\mathbf{r}$ . The random rotation angle  $\Delta \phi$  is selected with uniform probability from some interval  $[-\lambda, \lambda]$ . Finally, the projection  $\mathbf{r}_\perp$  of the vector  $\mathbf{r}$  into the plane perpendicular to  $\mathbf{k}$  is rotated by  $\Delta \phi$  and the resultant vector connecting the pivot and the rotated monomer is given by  $\mathbf{r}'$ . A schematic depiction of the single-displacement and the pivot updates is provided in Fig. 3.5. It should be mentioned, that when used in simulations of polymer models with elastic bonds, the pivot update is not ergodic since it preserves bond length [1]. Therefore it is recommended to combine rotational updates with single displacement updates whenever applicable.

# Chapter 4

## Off-Lattice Polymer Models

It is hardly possible to overestimate the importance of defining an appropriate model to represent a real physical system in a computational study. What constitutes an ‘appropriate’ model depends largely on the system under investigation and on the level of detail which is needed to correctly capture the properties of a given physical phenomena. For example, the study of chemical reaction kinetics, ground-state geometries of molecules, or the optical and electronic properties of semiconductors, requires detailed knowledge of the electronic structure and interactions. In such cases, Density functional theory (DFT) [37] or other quantum mechanical modelling methods need to be employed. On the other hand, a wide range of interesting physical phenomena, such as protein folding, polymer collapse, adsorption, and aggregation, are driven by cooperative structure forming processes and as such are not expected to depend sensitively on the precise electronic or even atomic structures. In principle, it is possible to gain insight into these processes by the means of simplified models with a reduced number of effective parameters [1, 38]. In this chapter we shall briefly discuss the concept of *coarse-graining* and introduce the model for the flexible elastic homopolymer together with a set of structural order parameters which are particularly effective at characterizing the conformational geometries of polymers in the solid pseudophase.

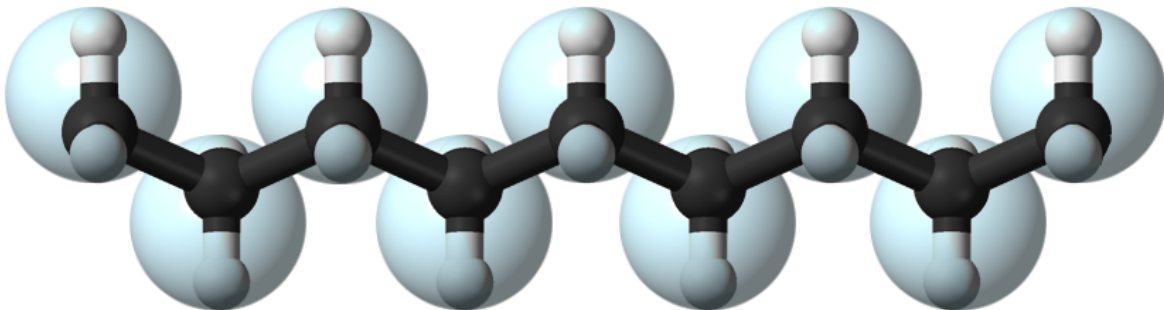


Figure 4.1: An example of a coarse-grained model of polyethylene. Methylene groups ( $\text{CH}_2$ ) are replaced by coarse-grained interaction sites which are depicted as transparent spheres. The interactions between the sites are described in terms of effective potentials.

## 4.1 Coarse-grained models

The general idea behind coarse-graining is the observation that for a wide range of physical phenomena the individual degrees of freedom of a system do not act independently but rather behave in a cooperative fashion. The goal is then to find the minimal set of degrees of freedom which would allow for an accurate description of a given physical process. In the context of biomolecules, this typically amounts to replacing individual atoms by coarse-grained interaction sites and exact quantum many-body interactions by effective potentials [Fig. 4.1]. The new interaction sites are often referred to as *monomers*.

Individual conformations of a coarse-grained model with  $N$  monomers can be represented by a  $3N$ -dimensional vector  $\mathbf{Q} = (q_1, q_2, \dots, q_{3N})$  in the reduced coordinate system. The components  $q_i$  represent the relevant degrees of freedom and are defined in terms of the map

$$\tilde{q}_i(\mathbf{X}) : \mathbf{X} \rightarrow \mathbf{Q} \quad (4.1)$$



between the full conformational space  $\mathbf{X}$  and the reduced space  $\mathbf{Q}$ . In the full conformational space, the canonical partition function is defined as

$$Z_{\text{can}} = \int \mathcal{D}\mathcal{X} e^{-\beta V(\mathbf{X})}, \quad (4.2)$$

where  $V(\mathbf{X})$  is the exact inter-atomic potential. In order to express  $Z_{\text{can}}$  in terms of the coarse-grained coordinates, we begin by integrating out the microscopic degrees of freedom

$$Z_{\text{can}} = \int \mathcal{D}\mathcal{Q} \int \mathcal{D}\mathcal{X} \prod_{i=1}^{3N} [\delta(q_i - \tilde{q}_i(\mathbf{X}))] e^{-\beta V(\mathbf{X})}. \quad (4.3)$$

Next we replace  $V(\mathbf{X})$  by an effective potential

$$\tilde{V}(\mathbf{Q}) = -k_{\text{B}} T \ln \int \mathcal{D}\mathcal{X} \prod_{i=1}^{3N} [\delta(q_i - \tilde{q}_i(\mathbf{X}))] e^{-\beta V(\mathbf{X})}. \quad (4.4)$$

and write

$$Z_{\text{can}} = \int \mathcal{D}\mathcal{Q} e^{-\beta \tilde{V}(\mathbf{Q})}. \quad (4.5)$$

In principle,  $\tilde{V}(\mathbf{X})$  contains the combined effects of the exact inter-atomic potentials and hence should allow for an accurate description of the thermodynamic and structural properties of the original system. However in reality, effective potentials are often only crude approximations to the definition introduced in Eq. 4.4. The perhaps surprising fact, that a wide range of physical phenomena can be studied by the means of drastically simplified models, suggests that physical properties that arise through cooperative behaviors do not depend sensitively on microscopic details.

## 4.2 Flexible elastic homopolymer

The generic model of a flexible, elastic, homopolymer is suitable for the investigation of the thermodynamic properties of polymer chains on a coarse-grained level. The polymer is represented by a linear chain of elastically bonded coarse-grained interaction sites, i.e., monomers [Fig. 4.3]. Individual monomers have neutral electric charges and do not interact via Coulomb forces. Instead, all structure forming processes are primarily driven by effective dipole-dipole interactions represented by the van Der Waals forces.

The potential energy of a dipole-dipole interaction between a pair of monomers  $(i, j)$  separated by the distance  $r$  is given by

$$V_{\text{dip}}(r) = \frac{1}{4\pi\epsilon_0} \frac{1}{r^3} [\mathbf{p}_i \cdot \mathbf{p}_j - 3(\mathbf{p}_i \cdot \hat{\mathbf{r}})(\mathbf{p}_j \cdot \hat{\mathbf{r}})], \quad (4.6)$$

where  $\mathbf{p}_i$  is the dipole moment of the  $i$ th monomer and  $\hat{\mathbf{r}}$  is the unit vector in the direction given by the separation vector between the two monomers [39]. However the strength of the potential decreases with the third power of the distance which is not consistent with the  $1/r^6$  decay typically observed in experiments. In fact, the problem must be treated quantum mechanically to account for the existing overlap between electron wave functions. The potential  $V_{\text{dip}}(r)$  is replaced by a dipole-dipole operator  $\hat{H}_{\text{dip}}$ , which is then introduced as a perturbation to a system of two non-interacting monomers. The first non-trivial term in the perturbation expansion of the ground state energy yields the desired  $1/r^6$  dependence [1]. In addition to this generic long range attraction, interacting bodies experience strong short range repulsion due to repelling electronic clouds. Both effects are contained in the famous Lennard-Jones potential [40]

$$U_{\text{LJ}}(r_{ij}) = 4\epsilon \left[ \left( \frac{\sigma}{r_{ij}} \right)^{12} - \left( \frac{\sigma}{r_{ij}} \right)^6 \right], \quad (4.7)$$

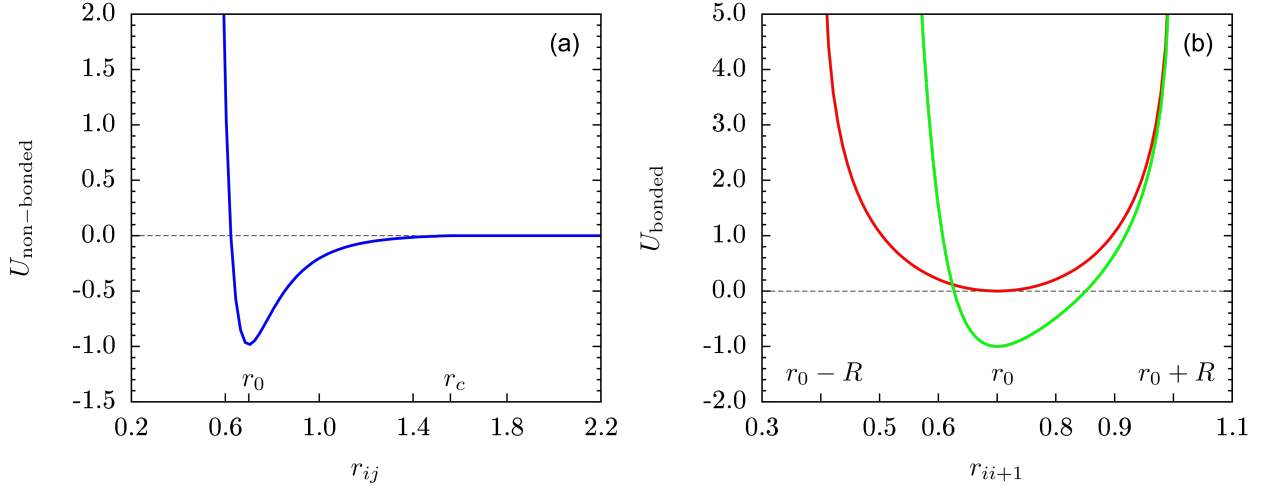


Figure 4.2: (a) Non-bonded interactions in the generic model of an elastic homopolymer are represented by the Lennard-Jones potential. Interacting monomers experience strong repulsion below the equilibrium distance  $r_0$ , and are weakly attracted over the interval  $(r_0, r_c)$  where  $r_c$  marks the cutoff distance. (b) The nonlinear FENE potential (red) is a symmetric representation of the bonded interactions. As a possible variant, the symmetry of the bonded potential can be broken by combining the FENE and the Lennard-Jones potentials (green).

where  $\epsilon$  sets the energy scale of the interaction while the relevant length scale is given by the van der Waals distance  $\sigma$  [Fig. 4.2(a)].

The bonds between adjacent monomers are represented by an elastic potential which allows for longitudinal bond vibrations. The simplest approximation is given by the harmonic spring potential (Rouse model), however the linearity of the interaction force allows for large separation between the bonded monomers. This problem can be avoided by introducing a potential which diverges for  $|r - r_0| \geq R$ , where  $r_0$  is the equilibrium bond length and  $R$  controls the allowed fluctuation width. A particularly suitable choice is the finitely extensible nonlinear elastic (FENE) potential [Fig. 4.2] [41–43]

$$U_{\text{FENE}}(r_{ii+1}) = -\frac{K}{2}R^2 \ln \left[ 1 - \left( \frac{r_{ii+1} - r_0}{R} \right)^2 \right]. \quad (4.8)$$

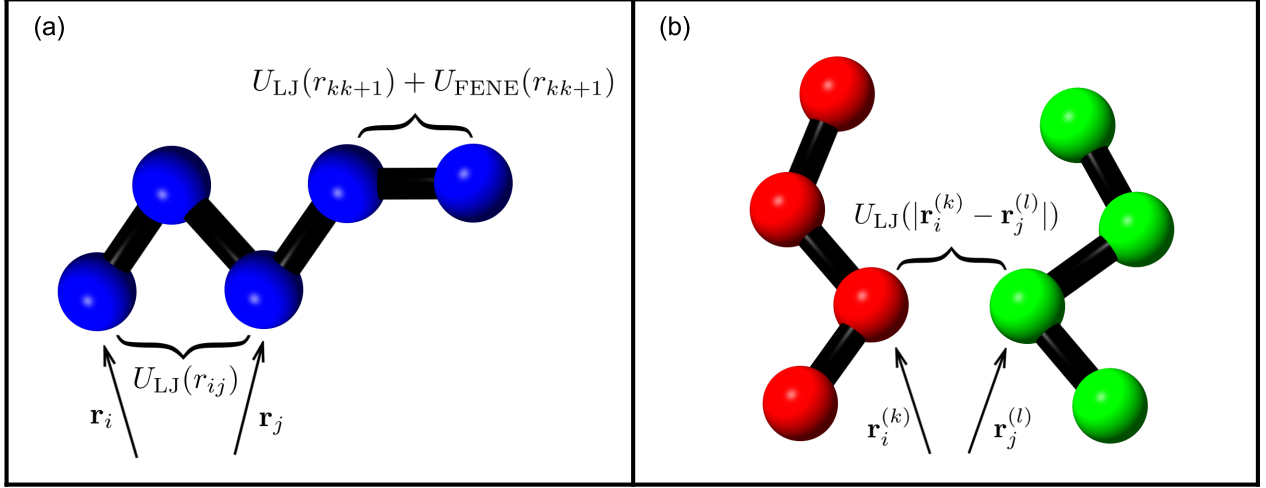


Figure 4.3: (a) Generic model of a flexible elastic homopolymer. All monomers interact via a pairwise Lennard-Jones potential (LJ). Bonded interactions include an additional finitely extensible nonlinear elastic potential (FENE). (b) In a multi-chain system, the interactions between monomers belonging to different chains are also represented by the (LJ) potential.

### 4.2.1 Single elastic chain

In the following, we will define the model for a single elastic polymer chain which will be used for the remainder of this thesis [Fig. 4.3]. The specific values of the model parameters will be provided individually in the later chapters. The energy of a polymer chain of length  $N$  in a conformation  $\mathbf{X} = (\mathbf{r}_1, \dots, \mathbf{r}_N)$  is given by the sum of non-bonded and bonded contributions

$$E(\mathbf{X}) = \sum_{i < j+1}^N U_{\text{non-bonded}}(r_{ij}) + \sum_{i=1}^{N-1} U_{\text{bonded}}(r_{ii+1}). \quad (4.9)$$

All non-bonded interactions are represented by the Lennard-Jones potential introduced in Eq. 4.7. In order to reduce the number of required calculations in a computer simulation, it is a standard procedure to introduce a cutoff distance  $r_c$  and set  $U_{\text{LJ}} = 0$  for all  $r \geq r_c$ . The truncated LJ potential must also be shifted vertically by the constant  $U_{\text{LJ}}(r_c)$  to prevent

a discontinuity at  $r_c$ . Hence the non-bonded interactions are represented by

$$U_{\text{non-bonded}}(r_{ij}) = U_{\text{LJ}}^{\text{trunc}}(r_{ij}) = \begin{cases} U_{\text{LJ}}(r_{ij}) - U_{\text{LJ}}(r_c), & r_{ij} \leq r_c, \\ 0, & r_{ij} > r_c. \end{cases} \quad (4.10)$$

In addition to the FENE potential [Eq. 4.8], bonded interactions contain an additional Lennard-Jones term

$$U_{\text{bonded}}(r_{ii+1}) = U_{\text{FENE}}(r_{ii+1}) + U_{\text{LJ}}^{\text{trunc}}(r_{ii+1}). \quad (4.11)$$

The short range repulsive part of the LJ potential ensures that the resultant potential is asymmetric. The shapes of the bonded and non-bonded potentials are shown in Fig. 4.2.

### 4.2.2 Interacting elastic chains

A system of interacting elastic homopolymer chains is a suitable model for the study of generic features of macromolecular aggregation. The energy of  $M$  interacting chains, each consisting of  $N$  identical monomers, can be separated into intra-chain and inter-chain pairwise interactions

$$E_{\text{total}} = E_{\text{intra}} + E_{\text{inter}}. \quad (4.12)$$

The intra-chain contribution

$$E_{\text{intra}} = \sum_{k=1}^M \sum_{i=1}^{N-1} U_{\text{bonded}}(r_{ii+1}^{(k)}) + \sum_{k=1}^M \sum_{i < j}^N U_{\text{non-bonded}}(r_{ij}^{(k)}) \quad (4.13)$$

consists of both bonded and non-bonded interactions, as defined in Sec. 4.2.1, and  $r_{ij}^{(k)}$  is the distance between the pair of monomers  $(i,j)$  of the  $k$ -th chain. The inter-chain contribution

$$E_{\text{inter}} = \sum_{k < l}^M \sum_{i,j}^N U_{\text{LJ}}^{\text{trunc}}(|\mathbf{r}_i^{(k)} - \mathbf{r}_j^{(l)}|), \quad (4.14)$$

consists solely of non-bonded Lennard-Jones interactions. Schematic depiction of the model is provided in Fig. 4.3 (b).

### 4.3 Structural order parameters

The formalism of the microcanonical inflection-point analysis, as introduced in section 2.1.2, provides a systematic approach for the identification and classification of pseudophase transitions in mesoscopic systems. Further insight into the thermodynamic and structural properties of polymer systems can be obtained by identifying the set of conformations which are dominant in a given pseudophase. This can be accomplished either by visual inspection of sample structures, or more systematically, by introducing a suitable set of structural order parameters.

An example of a useful and easily computable structural quantity is the radius of gyration

$$r_{\text{gyr}}(\mathbf{X}) = \sqrt{\frac{1}{N} \sum_{i=1}^N (\mathbf{r}_i - \mathbf{r}_{\text{com}})^2}, \quad (4.15)$$

where

$$\mathbf{r}_{\text{com}} = \frac{1}{N} \sum_{i=1}^N \mathbf{r}_i \quad (4.16)$$

is the center-of-mass of the polymer conformation. The average  $\langle r_{\text{gyr}} \rangle$  is a measure of the compactness of the dominant conformations found at a given canonical temperature.

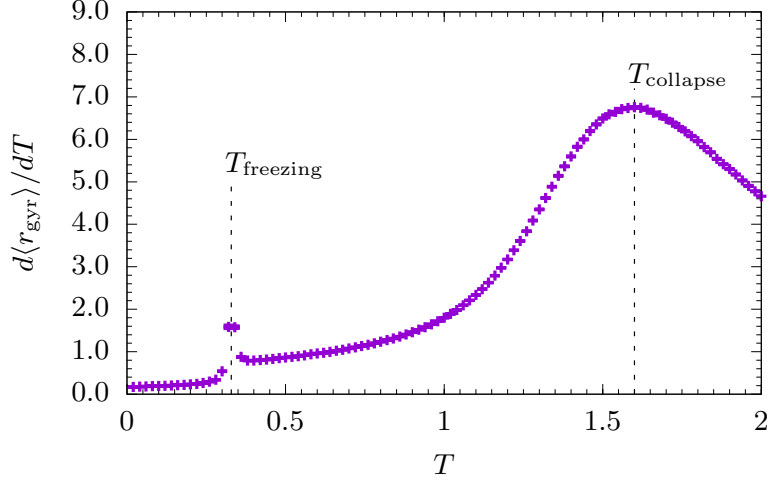


Figure 4.4: The thermal fluctuations of the radius of gyration obtained from a Monte Carlo simulation of an elastic 55mer. The distinct peaks indicate the locations of the freezing and collapse transitions at the temperatures  $T_{\text{freezing}}$  and  $T_{\text{collapse}}$  respectively.

Signals, such as peaks and shoulders, in the temperature derivative

$$\frac{d\langle r_{\text{gyr}} \rangle}{dT} = \frac{\langle r_{\text{gyr}} E \rangle - \langle r_{\text{gyr}} \rangle \langle E \rangle}{k_B T^2} \quad (4.17)$$

indicate locations of heightened thermodynamic activity and are routinely used to identify pseudophase transitions [Fig. 4.4].

Alternatively, a wide range of polymer conformation geometries can be identified using the set of rotationally invariant order parameters

$$Q_l = \left[ \frac{4\pi}{2l+1} \sum_{m=-l}^l |\rho_{l,m}|^2 \right]^{1/2}, \quad (4.18)$$

where

$$\rho_{l,m} = \frac{1}{N} \sum_{i=0}^N Y_{l,m}(\mathbf{r}_i) \quad (4.19)$$

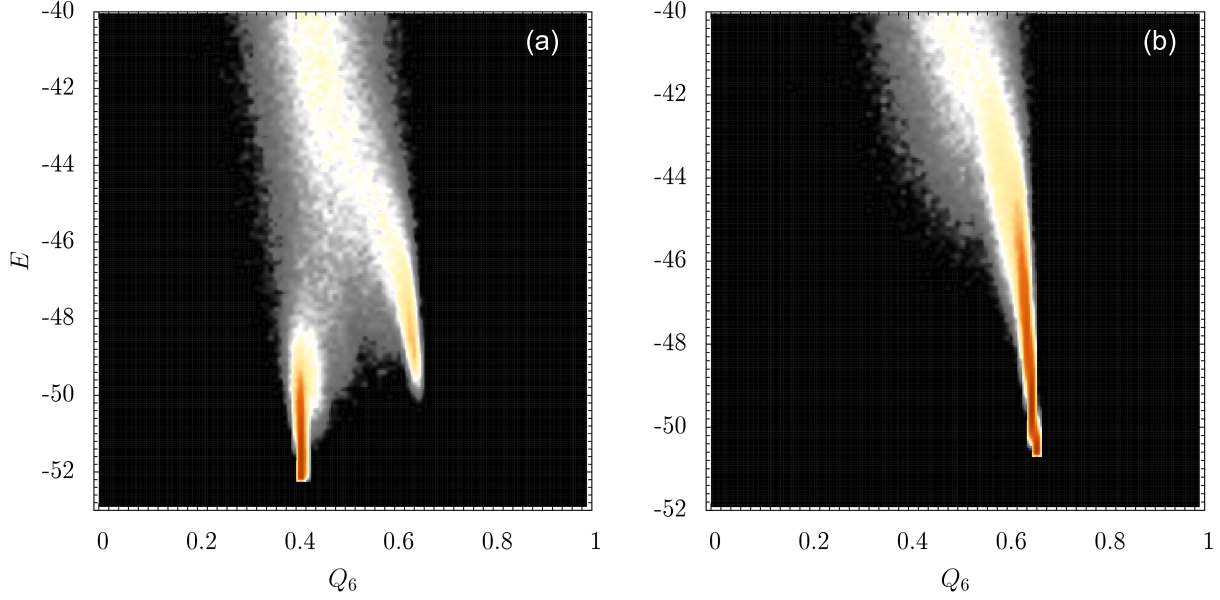


Figure 4.5: Intensity plots of the rotationally invariant order parameter  $Q_6$  for two variants of a coarse-grained model of an elastic 15mer. The shading indicates the probability of detecting a configuration with a given value of the order parameter, red being the maximum probability and black being the lowest. In figure (a), the two prominent low energy branches reveal the existence of two solid pseudophases with distinct conformational geometries. Whereas in (b), only a single solid phase is detected.

is the average of the real spherical harmonics<sup>1</sup> evaluated at positions of the individual monomers [44]. This set of order parameters has been particularly useful in the investigations of polymer systems exhibiting multiple solid pseudophases at low energies [45]. In Fig. 4.5 we provide an illustration of this approach as applied to two different variants of a coarse-grained model of an elastic 15mer.

<sup>1</sup>The real harmonics can be expressed in terms of the better known complex harmonics as

$$Y_{lm}(\mathbf{r}_i) = \begin{cases} \frac{i}{\sqrt{2}} [Y_l^m(\mathbf{r}_i) - (-1)^m Y_l^{-m}(\mathbf{r}_i)] & \text{if } m < 0, \\ Y_l^m(\mathbf{r}_i) & \text{if } m = 0, \\ \frac{1}{\sqrt{2}} [Y_l^{-m}(\mathbf{r}_i) + (-1)^m Y_l^m(\mathbf{r}_i)] & \text{if } m > 0. \end{cases} \quad (4.20)$$



# Chapter 5

## Confinement Effects upon Structural Transitions in Elastic Polymer Chains

In chapter 4, we have suggested that the structural and thermodynamic properties of polymer systems can be investigated by the means of rather simple coarse-grained models. It is desirable that the general features of the model, such as the types of observed pseudophases and low energy conformational geometries, remain at least qualitatively similar over a range of model parameters. In recent studies, the effect of the interaction range between non-bonded monomers of a single elastic homopolymer has been addressed systematically [46–48]. It has been found that for sufficiently short interaction ranges, it is possible for the polymer to fold directly from random-coil structures (i.e., the gas phase) into solid and compact conformations. Under these conditions, no globular (or liquid) phase is present.

In this chapter, we investigate the effects of restricting the fluctuation range of bonded interactions on the structural and thermodynamic properties of a single elastic polymer chain. The variation of the bond extension range allows us to bridge the gap between self-interacting polymers with stiff bonds (such as proteins) and bead-spring chains (elastic polymers) with bonds so floppy that these polymers behave similarly to a gas of interacting

particles. For this purpose, we have performed extensive replica-exchange Monte Carlo simulations in extended multiple Gaussian modified ensembles [22], which help improve the efficiency of parallel tempering simulations near first-order transitions. Systematic studies of the structural phases in the space of the bond confinement parameter were made possible by employing standard canonical analyses of fluctuations in macroscopic thermodynamic quantities and also by careful analysis of the nature of inflection points in the microcanonical temperature curve [1,8].

## 5.1 Model and simulation parameters

In this study, we employ a coarse-grained model of an elastic homopolymer, in the same form as introduced in Sec. 4.2.1. This model was originally introduced for investigations of general properties of elastic polymer chains. Due to the similarity in the transition behavior of atomic clusters and polymers, however, the scope of this model can be extended to investigate effects of bond confinement as well. As such, this model allows for the interpolation of systems ranging from polymers to an almost unconfined gas of atoms.

The energy and the length scales of the truncated and shifted Lennard-Jones potential (Eq. 4.10) were set to  $\epsilon = 1$  and  $\sigma = r_0/2^{1/6}$  respectively, where  $r_0 = 0.7$  marks the location of the minimum potential. The cut-off radius was set at  $r_c = 2.5\sigma$  such that  $U_{\text{LJ}}(r_c) \approx -0.0163169\epsilon$ . The FENE potential (Eq. 4.8), which together with the LJ potential represents bonded interactions, is used here in the modified form

$$U_{\text{FENE}}(r_{ii+1}) = -\frac{K}{2}R_0^2 \ln \left[ 1 - \left( \frac{r_{ii+1} - r_0}{R} \right)^2 \right], \quad (5.1)$$

where  $K = 40$  and  $R_0 = 0.3$ . The parameter  $R$  inside of the logarithmic term controls the effective confinement range of the polymer bonds, whereas the energy scale of the potential is

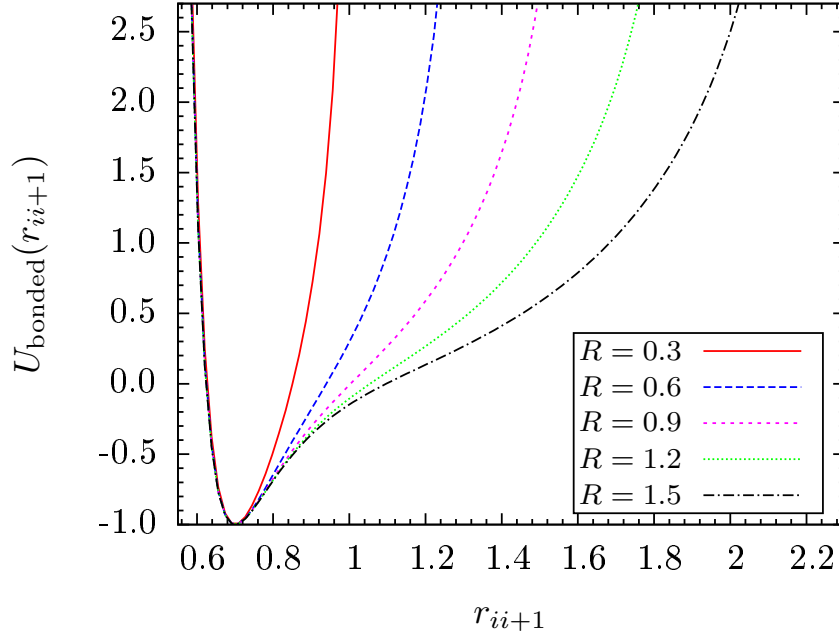


Figure 5.1: Behavior of the combined bond potential  $U_{\text{bonded}}(r_{ii+1}) = U_{\text{LJ}}(r_{ii+1}) + U_{\text{FENE}}(r_{ii+1})$  for different values of the effective bond confinement range  $R$ .

kept constant. The qualitative behavior of the combined bond potential for different values of  $R$  is shown in Fig. 5.1. The bond elasticity increases with  $R$ , i.e., by changing  $R$  in a wide range of values ( $R \in [0.3, 90]$ ), we systematically investigate an entire class of polymer systems between the limits of stiff polymers ( $R \rightarrow 0$ ) and, effectively, a gas of nonbonded Lennard-Jones particles, for which  $R \rightarrow \infty$ .

In our simulations, we have used the replica-exchange Monte Carlo<sup>1</sup> (parallel tempering) [18–21], extended to multiple Gaussian modified ensembles<sup>2</sup> (MGME) [22]. The typical number of replicas in a simulation was  $\sim 80$ , covering the temperature range  $T \in [0.02, 2.0]$ . The total number of Monte Carlo sweeps per simulation totalled  $5 \times 10^8$ . A replica exchange update was attempted every 100 Monte Carlo sweeps and accepted at an average

<sup>1</sup>See also section 3.1.2

<sup>2</sup>See also section 3.1.3

rate exceeding 20%. The acceptance rates for Metropolis updates in each thread was kept at  $\sim 40 - 60\%$ . Simulations were carried out on a two-dimensional mesh of temperatures and  $E_G$  values in the first-order transition region. On average 10 different values of  $E_G$  were used per temperature thread. The system was constrained inside of a steric sphere at a constant density of 0.001 particles per unit volume, in which case the diameter of the sphere is larger than the length of the fully extended chain. Under these conditions, we consider the system to be highly dilute.

The results presented in this chapter are compared for classes of polymers with  $N = 13$  and 30 monomers. For verification purposes, we have also studied polymers with up to 55 monomers, which, for this kind of systematic study that covers the entire parameter space, represents the limit of currently feasible simulations.

## 5.2 Results

In this section, we investigate the influence of the confinement parameter  $R$  on the structural transitions in elastic chains of lengths  $N = 13$  and 30 in the dilute regime. For this purpose, we first perform a conventional canonical statistical analysis of fluctuating quantities and compare with results of a corresponding microcanonical analysis.

### 5.2.1 Canonical analysis of energetic and structural fluctuations

For the identification of transition points, we first consider the changes in the thermodynamic behavior of energetic and structural canonical fluctuation quantities. The transition behavior is compared for various values of the confinement parameter  $R$ . This analysis enables us to construct a structural hyperphase diagram. Differences in the overall generic transition behavior are discussed for two system sizes ( $N = 13, 30$ ).

The statistical fluctuation of a thermodynamic quantity  $O$  is defined by the temperature derivative of its expectation value

$$\langle O(\mathbf{X}) \rangle(T) = \frac{1}{Z(T)} \int \mathcal{D}X O(\mathbf{X}) e^{-E(\mathbf{X})/k_B T}, \quad (5.2)$$

where  $\mathcal{D}X$  is the integral measure in the space of all polymer conformations  $\mathbf{X}$  and

$$Z(T) = \int \mathcal{D}X e^{-E(\mathbf{X})/k_B T} \quad (5.3)$$

is the partition function of the canonical ensemble of these structures at the canonical (heat-bath) temperature  $T$ . Thus, changes in the monotonous behavior of

$$\begin{aligned} \frac{d}{dT} \langle O(\mathbf{X}) \rangle(T) &= \frac{1}{k_B T^2} \\ &\times [\langle O(\mathbf{X}) E(\mathbf{X}) \rangle(T) - \langle O(\mathbf{X}) \rangle(T) \langle E(\mathbf{X}) \rangle(T)] \end{aligned} \quad (5.4)$$

indicate pronounced thermal activity of the system. The most common and easily accessible quantity in Monte Carlo simulations is the specific heat, which represents the fluctuations of energy<sup>3</sup>. In this case  $O = E$  and

$$c_V(T) = \frac{1}{N} \frac{d}{dT} \langle E(\mathbf{X}) \rangle(T). \quad (5.5)$$

The thermal fluctuations of the energy (specific heat) and of the radius of gyration<sup>4</sup> of 13mers and 30mers are shown in Fig. 5.2, for different values of bond confinement ranges  $R$ . Generally, peaks and “shoulders” in these quantities indicate locations of structural transitions. The generic transitions of elastic chains are the  $\Theta$  collapse transition that separates the gas-like phase of random-coil conformations from the liquid, collapsed globular phase,

---

<sup>3</sup>See also section 2.2

<sup>4</sup>Radius of gyration was introduced in section 4.3.

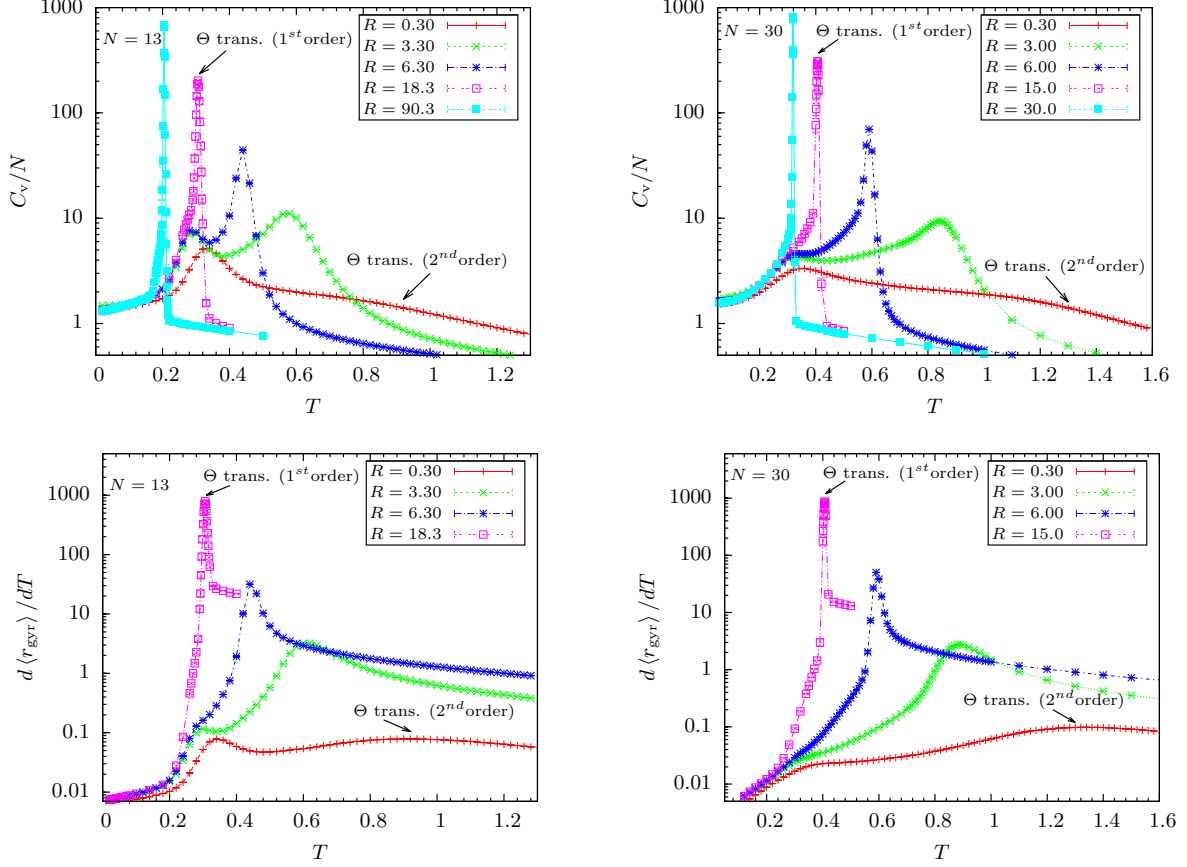


Figure 5.2: Specific heat and the thermal fluctuations of the radius of gyration for 13mers and 30mers, parametrized by the bond confinement parameter  $R$ .

and the freezing transition from the globular into the solid “crystalline” phase [49,50]. Interestingly, previous studies have shown that both transitions merge if *nonbonded* interactions are restricted to extremely short-ranges [46–48]. We have observed similar behavior in systems where extremely large bond fluctuations are allowed. Whereas, with increasing values of  $R$ , the low-temperature signal in the specific-heat curves in Fig. 5.2 (which, for example, for  $R = 3.0$  is still clearly associated with the freezing transition) shifts only slightly to lower temperatures, the  $\Theta$  transition signal drops significantly and finally merges with the freezing transition at  $R \sim 30$ . Whether the freezing and  $\Theta$  transitions remain well separated for

all values of  $R < 30$  cannot be unambiguously determined by inspection of the canonical fluctuation quantities, in particular since for  $R > 15$  the freezing transition signal turns into a shoulder on the low-temperature flank of the more dominant  $\Theta$  transition peak. We will provide evidence for the separation of the transitions, using the methods of microcanonical analysis in the next section.

The general properties of the freezing transition do not change noticeably until its merger with the  $\Theta$  transition. This is plausible since the freezing transitions are driven mainly by the Lennard-Jones pair interactions between bonded and nonbonded monomers that optimize the icosahedral-like conformations in the solid phase. Therefore, this transition is not significantly affected by the modifications in the bond elasticity.

In the solid phase, the “magic” 13mer possesses a perfect icosahedral shape [49, 50], whereas the 30mer forms amorphous structures. The energy histograms of the 13mer exhibit bimodal shapes near the freezing transition point for values of  $R < 30$ , suggesting a first-order-like transition of the finite system. The “liquid-solid” transition of the 30mer resembles a “liquid-liquid” transition, since the compact globular conformations are difficult to distinguish from the amorphous solid structures. Nonetheless, the transition signal is clearly visible and the unimodal shape of the canonical energy histograms (not shown) in this region of  $R$  space indicates a second-order-like transition.

More striking is the dramatic change of the characteristic features of the  $\Theta$  transition. As expected, for  $R \sim 0.3$ , the transition is still *second-order-like* [51, 52]. In the specific heat-curves in Fig. 5.2 it is clearly visible that with increasing values of  $R$ , the shoulders indicating the  $\Theta$  transitions turn into distinct peaks which rapidly become narrower and more pronounced as they shift to lower temperatures. For values of  $R > 4.5$ , the canonical energy histograms obtained at the transition temperature are no longer unimodal, which suggests that the  $\Theta$  transition become *first-order-like*. This can be seen nicely in Fig. 5.3, where energy histograms for the 13mer with  $R = 15$  at temperatures near the  $\Theta$  transition

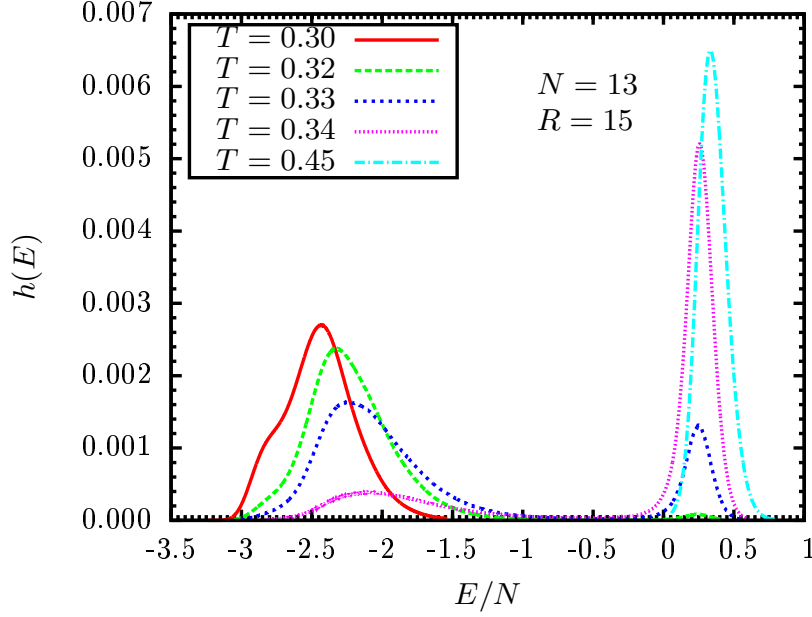


Figure 5.3: Energy histograms of the 13mer with  $R = 15$  at several temperatures near the  $\Theta$  point. The bimodal shape of the histograms near the transition temperature  $T_\theta = 0.331$  clearly indicates a first order pseudophase transition.

point are shown. For temperatures near  $T = 0.33$ , the bimodal shape of the histograms is clearly visible. The phase separation between gas and liquid is unusual for a polymer and indicates that for  $R = 15$  the particles in the system are quasi-free and behave rather like a loosely confined interacting gas, because bond-crossings are possible. The disappearance of the two distinct transition signals for  $R > 30.0$  marks the end of existence of a separate liquid phase. This behavior is similar for both systems sizes studied and might be universal. However, the strikingly prominent signals for the  $\Theta$  transition and the disappearance of the liquid phase are limited to the dilute regime and would not be observed at higher particle densities [53, 54]. It should be mentioned that the phase separation becomes substantially stronger for larger  $R$  values, as well as the interfacial surface tension due to the radical entropic depletion in the energetic gap region.



With the transition temperatures obtained from the peaks in the canonical quantities we construct structural phase diagrams parametrized by the temperature  $T$  and the confinement parameter  $R$ . For both system sizes, near the unmodified values of  $R$ , we observe three distinct structural phases. The high-temperature curves in Fig. 5.4 represent the  $\Theta$  transition lines, at which the expanded coils in the gas phase collapse into the compact but disordered globular states in the liquid phase. The green and red portions of the  $\Theta$  transition line indicate the regions in which the transition is second-order-like and first-order-like respectively. The merging of the freezing and the  $\Theta$  lines indicates the absence of the liquid phase and a direct transition from the gas to the crystalline phase for values of  $R > 30$ . The apparent similarities between the phase diagrams in the  $\Theta$  regime suggest that similar behavior in systems of larger sizes could be expected. The different order of the liquid-solid transition (first order for the 13mer and second order for the 30mer) is a consequence of the entropic character of the solid phase. For the 13mer, the icosahedron is the all dominating morphology with comparatively low entropy and specific energy that sets apart the liquid phase and creates a phase-separation scenario. On the other hand, the “solid” phase of the 30mer is of rather highly entropic amorphous nature and allows for a continuous crossover from the liquid phase.

It is instructive to consider the effects of the bond confinement range on ground state conformations. It was previously shown [48] that a decrease in the interaction range of the Lennard-Jones potential can lead to the disappearance of icosahedral ground-state structures in “magic” system sizes (such as  $N = 55$ ). In the present study, the ground state energies remained virtually constant and the conformations of 13mers retained their icosahedral geometry even for extremely high values of the parameter  $R$ . This suggests that the low-temperature behavior of flexible homopolymer chains is dominated by Lennard-Jones interactions while the FENE potential influences only the particular orderings of monomers within the ground-state structures.

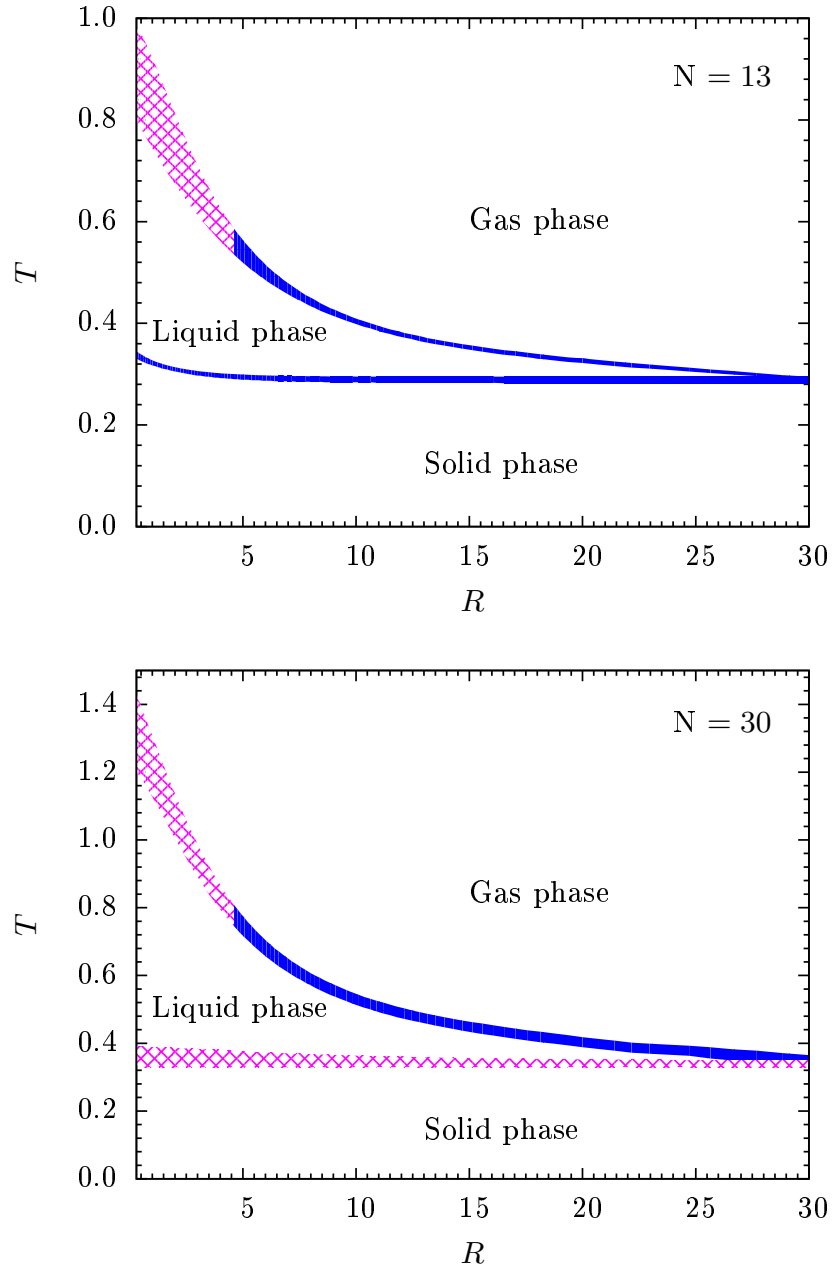


Figure 5.4: Structural phase diagrams for 13mers and 30mers, parametrized by the canonical temperature  $T$  and the confinement parameter  $R$ . The blue (solid) and pink segments indicate first-order-like and second-order-like transitions, respectively.

### 5.2.2 Results of microcanonical inflection-point analysis

As discussed in the previous section, the results obtained by means of canonical analysis suggest that the  $\Theta$  transition acquires first-order-like character in systems with large bond confinement range. However, the analysis of structural transitions based on canonical quantities is often ambiguous. Canonical energy histograms are useful for determining the order of a transition only if their shape is clearly bimodal or unimodal. In this section, we turn to microcanonical inflection-point analysis<sup>5</sup> which offers a robust and unambiguous approach towards the classification of structural transitions [1, 8, 28].

In Fig. 5.5 we summarize the results for chains of lengths with  $N = 13$  and 30 monomers for values  $R = 0.3, 4.5, 30.0$ . In addition to the microcanonical temperature  $\beta(E)$  and its first derivative  $\gamma(E) = d\beta/dE$ , we also plot the canonical energy histograms  $h(E)$  obtained at the  $\Theta$  transition temperature.

For  $R = 0.3$ , the negative valued peaks of  $\gamma(E)$  indicate that the  $\Theta$  transition is of second order, in agreement with the observation that the canonical energy histograms for both system sizes are clearly unimodal. At  $R = 4.5$ , the peaks of  $\gamma(E)$  become positive and we conclude that the  $\Theta$  transition turns to first order. The signals for freezing transitions remain well outside of the back-bending region of the  $\Theta$  transition, confirming that the two transitions are well separated.

In the case  $R = 30$ , the multiple peaks in  $\gamma(E)$  indicate that the  $\Theta$  transition consists of a hierarchy of subphase transitions. This is particularly apparent in nucleation transitions with entropy reduction due to stepwise loss of translational entropy. Prominent examples are aggregation transition in systems consisting of multiple polymer chains [1, 55–58], which will be discussed in detail in Chap. 7. The system undergoes a direct transition from the solid phase into the gas phase through a series of subphase transitions consisting of individual monomers breaking away from the bulk.

---

<sup>5</sup>See also section 2.1.2

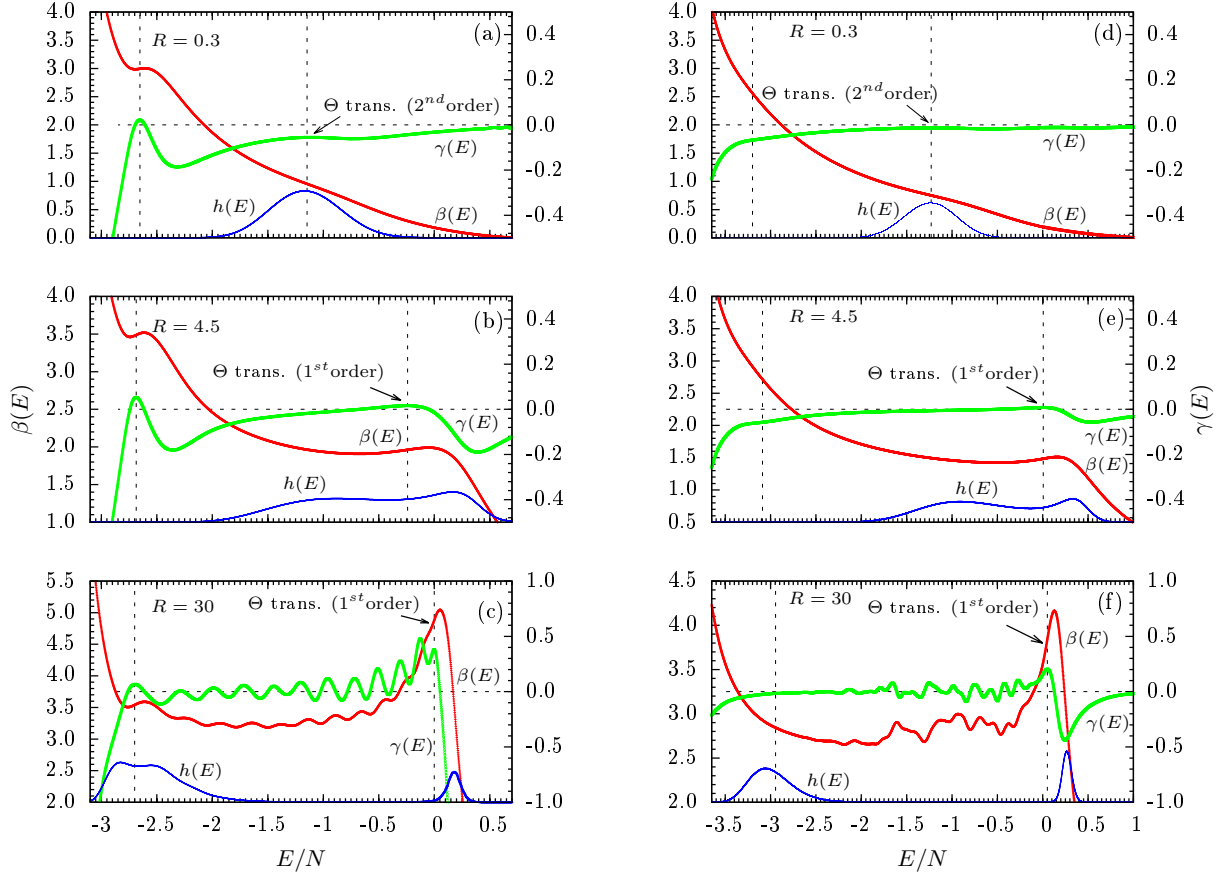


Figure 5.5: Microcanonical results for 13mers with bond confinement ranges (a)  $R = 0.3$ , (b) 4.5, and (c) 30 as well as for 30mers (d)-(f). Shown are inverse temperature curves  $\beta(E)$ , their first derivatives  $\gamma(E) = d\beta(E)/dE$ , and (on arbitrary scale) the energy histograms  $h(E)$  at the  $\Theta$  transition temperature. The horizontal dashed line marks  $\gamma = 0$ . The positive valued peaks of  $\gamma(E)$  for values of  $R > 4.5$  clearly indicate that the  $\Theta$  transition is first order, but remains separate from the freezing transition. The absorption of the freezing transition by the  $\Theta$  transition is apparent for large confinement ranges (c, f).

This can be seen nicely in the case of a 13mer with the confinement range  $R = 30$ . Shown in Fig. 5.5(c), each of the 12 oscillations in the back-bending region of  $\beta(E)$  corresponds to a subphase transitions. For a 30mer, at the same  $R$  value [Fig. 5.5(f)], subphases overlap to an extent that only an accumulated effect upon  $\beta(E)$  is visible.

The freezing transition is no longer an autonomous transition but instead becomes one of the subphase transitions that make up the  $\Theta$  transition. Eventually, this entails the absence of a separate liquid phase, which is in agreement with the overall picture obtained by the canonical analysis of fluctuating quantities.

The maximum  $R$  value is, of course, limited by the boundary of the simulation sphere that represents a steric constraint. The presence and the stability of the individual structural phases depend on the particle density. In the scenario presented here, where we investigate the disappearance of the liquid phase, we fixed the density to 0.001 particles per unit volume, whereas additional simulations at a 10 times larger density showed that the liquid phase remained stable, even for bond confinement ranges as large as  $R = 100$ . In the unconstrained case of open boundaries (which for fixed particle number means vanishing density) and  $R \rightarrow \infty$ , both liquid and solid phase are supposed to disappear and the gas phase would remain as the only stable phase. The disappearance of phases by reducing confinement has already been observed in atomic cluster systems some time ago [59, 60].

In Tables 5.1 and 5.2, we have listed the transition temperatures  $T_{f,\theta}$  and latent-heat values per monomer  $\Delta q_{f,\theta}$  for 13mers and 30mers at various bond confinement ranges  $R$ . Transition temperatures for the second-order transitions were obtained by microcanonical inflections-point analysis, whereas the transition points and latent heat values were estimated by means of microcanonical Gibbs construction.<sup>6</sup>

---

<sup>6</sup>For a description of the microcanonical Gibbs construction please refer to section 2.1.2.

Table 5.1: Microcanonical transition temperatures  $T_{f,\theta}$  and latent heats  $\Delta q_{f,\theta}$  at the freezing and  $\Theta$  transition points, respectively, for 13mers with different bond confinement ranges  $R$ .

$R$	$T_f$	$T_\theta$	$\Delta q_f$	$\Delta q_\theta$
0.3	$0.334 \pm 0.005$	$1.1 \pm 0.1$	$0.157 \pm 0.002$	N/A
1.5	$0.306 \pm 0.005$	$0.9 \pm 0.1$	$0.090 \pm 0.002$	N/A
3.0	$0.291 \pm 0.005$	$0.64 \pm 0.05$	$0.208 \pm 0.002$	N/A
4.5	$0.286 \pm 0.005$	$0.52 \pm 0.01$	$0.228 \pm 0.002$	$1.132 \pm 0.005$
9.0	$0.283 \pm 0.005$	$0.387 \pm 0.005$	$0.249 \pm 0.002$	$2.133 \pm 0.002$
15.0	$0.282 \pm 0.005$	$0.331 \pm 0.005$	$0.254 \pm 0.002$	$2.485 \pm 0.002$
30.0	$0.282 \pm 0.005$	$0.284 \pm 0.005$	$0.285 \pm 0.002$	$2.978 \pm 0.002$

Table 5.2: Same as Table 5.1, but for 30mers.

$R$	$T_f$	$T_\theta$	$\Delta q_f$	$\Delta q_\theta$
0.3	$0.39 \pm 0.01$	$1.3 \pm 0.1$	N/A	N/A
1.5	$0.39 \pm 0.01$	$1.2 \pm 0.1$	N/A	N/A
3.0	$0.38 \pm 0.01$	$0.88 \pm 0.05$	N/A	N/A
4.5	$0.37 \pm 0.01$	$0.69 \pm 0.01$	N/A	$1.650 \pm 0.005$
9.0	$0.36 \pm 0.01$	$0.496 \pm 0.005$	N/A	$2.647 \pm 0.002$
15.0	$0.35 \pm 0.01$	$0.416 \pm 0.005$	N/A	$3.057 \pm 0.002$
30.0	$0.35 \pm 0.01$	$0.344 \pm 0.005$	N/A	$3.399 \pm 0.002$

### 5.3 Summary

In this chapter, we have investigated the thermodynamic behavior of a linear chain of monomers connected by confined bonds which resembles a polymer for a large range of values of the bond confinement range  $R$ . Advanced parallel replica-exchange Monte Carlo methods, such as the Multiple Gaussian modified ensemble (MGME), were utilized in order to overcome the computational difficulties posed by the strong first-order-like behavior associated with the  $\Theta$  transition at large  $R$  values. Using the results obtained from the specific heat and the thermal fluctuations of the radius of gyration, we have constructed and compared features of the structural hyperphase diagrams for 13mers and 30mers. For low and intermediate confinement ranges, three distinct structural phases separated by the

freezing and the  $\Theta$  transitions can be identified, in agreement with the expected behavior. With increasing values of the parameter  $R$ , however, the  $\Theta$  transition line shifts to lower temperatures and eventually merges with the freezing transition line, suggesting the absence of an independent liquid phase. Microcanonical inflection-point analysis provides conclusive evidence that the  $\Theta$  transition turns from second order to first order if the bond confinement range parameter  $R$  exceeds a threshold value. This change in the character of the  $\Theta$  transition is not influenced by the freezing transition, which in this part of the phase diagram is still well separated from the  $\Theta$  point. Increasing the confinement range further,  $\Theta$  and freezing transitions merge and exhibit clear indications of a hierarchical nucleation transition. In this regime, the beads are quasi-free and interact likewise with others, bonded or nonbonded. The still coupled system behaves like an atomic cluster in a dilute regime. The general structure of the hyperphase diagrams can be expected to remain qualitatively intact even for substantially larger systems. The only anticipated change is that the freezing transition is of first order for all system sizes with more than about 40 monomers [8].

Our systematic study covers the technologically and biologically interesting regime of polymer chains with bond elasticities ranging from stiff to highly elastic, which includes all realistic linear macromolecules, and extends into the space of confined systems that behave like atomic clusters. Since our results are supposed to be generic, they allow for a classification of the expected transition behavior on the basis of the effective bond confinement range of these systems.

# Chapter 6

## Impact of Bonded Interactions on the Ground-State Geometries of Flexible Homopolymers

In this paper, we consider a generic model of the flexible elastic homopolymer and examine the effects of adding an extra Lennard-Jones term to the bonded potential. The unexpected consequences for the ground-state structures highlight the importance of a careful choice of model parameters.

### 6.1 Model and Methods

We employ a generic model of a flexible elastic homopolymer to study the effects of the shape and width of the bonded potential on the formation of low-energy structures for a polymer chain with  $N = 15$  monomers. Finite-size effects are essential and the 15mer shows a particularly distinct and clear transition behavior, which makes it a perfect candidate for this systematic study.



Non-bonded interactions are represented by the truncated and shifted Lennard-Jones (LJ) potential

$$U_{\text{LJ}}^{\text{trunc}}(r_{ij}) = \begin{cases} U_{\text{LJ}}(r_{ij}) - U_{\text{LJ}}(r_c), & \text{if } r_{ij} \leq r_c, \\ 0, & \text{if } r_{ij} > r_c, \end{cases} \quad (6.1)$$

where

$$U_{\text{LJ}}(r) = 4\epsilon \left[ \left( \frac{\sigma}{r} \right)^{12} - \left( \frac{\sigma}{r} \right)^6 \right]. \quad (6.2)$$

The energy scale is set to  $\epsilon = 1$  and the van-der-Waals radius to  $\sigma = r_0/2^{1/6}$ , where  $r_0 = 1.0$  is the location of the potential minimum. We select a cut-off radius at  $r_c = 2.5\sigma$  and introduce a shift  $U_{\text{LJ}}(r_c) \approx -0.0163169\epsilon$  to avoid discontinuities in the potential. In our model, monomers adjacent in the linear chain interact via a modified bonded potential

$$U_{\text{B}}(r) = -\frac{1}{2}KR^2 \ln \left[ 1 - \left( \frac{r - r_0}{R} \right)^2 \right] + \eta(U_{\text{LJ}}(r) + \epsilon) - (\epsilon + U_{\text{shift}}), \quad (6.3)$$

where  $R = 3/7$  and  $K = 98/5$ . In addition to the standard anharmonic FENE (finitely extensible nonlinear elastic) potential [?, ?, ?], the modified potential contains an additional Lennard-Jones term adjusted by a bond flexibility control parameter  $\eta$ . The bonded potential is shifted by  $-(\epsilon + U_{\text{shift}})$  in order to match the minimum energy with the non-bonded interactions.

The maximum bond extension is limited by the FENE potential, which diverges as  $r \rightarrow r_0 \pm R$ . Increasing the value of  $\eta$  introduces asymmetry to the bonded potential and the energy cost associated with non-optimal bond lengths is increased. In particular, compressed bonds result in high energy penalties as  $\eta$  becomes large. The effects of different  $\eta$  values on the shape and width of the bonded potential is exhibited in Fig. 6.1. The total energy of a configuration  $\mathbf{X} = (\vec{r}_1, \dots, \vec{r}_N)$  with the monomer-monomer distances  $r_{ij} = |\vec{r}_i - \vec{r}_j|$  is given

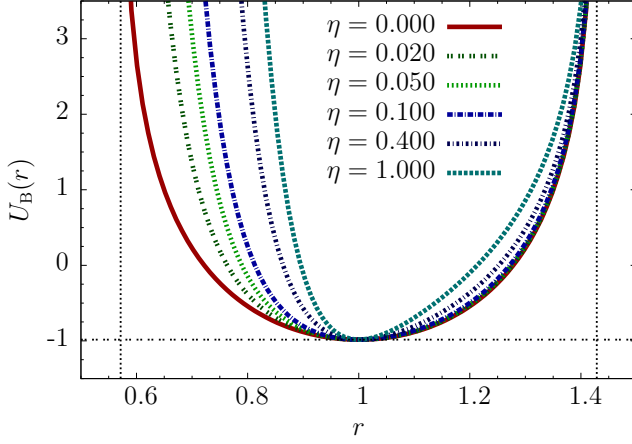


Figure 6.1: The modified bonded potential  $U_B(r)$ , modeled by the FENE and LJ interactions. The strength of the Lennard-Jones term is controlled by the bond flexibility parameter  $\eta \in [0, 1]$ .

by

$$E(\mathbf{X}) = \sum_{i < j}^N U_{\text{LJ}}(r_{ij}) + \sum_{i=1}^{N-1} U_B(r_{ii+1}). \quad (6.4)$$

In order to enhance the sampling of low-energy configurations, a parallel version of multicanonical sampling [?, ?, 25] is employed in this simulation. The standard multicanonical runs are performed in  $K$  replicas independently with the same initial weight functions but different random seeds. Displacement updates are proposed within a cubic box of edge lengths  $d = 0.3r_0$  and accepted according to the probability

$$P(X \rightarrow X') = \min[1, W(E(X'))/W(E(X))], \quad (6.5)$$

where  $W(E(X))$  represents the weight function of a given configuration  $X$ . After the  $i$ th iteration, since the weights are identical in each thread, the energy histograms obtained for each replica can simply be summed up:

$$H^i(E) = \sum_{k=1}^K H_k^i(E). \quad (6.6)$$

The total histograms are combined with the current weights to calculate the weights for the subsequent iteration by utilizing the error-weighted recursive scheme [?, 1, 25].

To construct the hyper-phase diagram, we use the generalized microcanonical inflection-point analysis [1, 8]. This approach has the advantage of uniquely and systematically locating the transition energies and thus is commonly employed to study pseudophase transitions in finite-size systems. By applying the principle of minimal sensitivity [?] to the derivatives of microcanonical entropy  $S(E)$ , the  $(2n + 1)$ th-order transition ( $n$  is a positive integer) is identified from the least sensitive inflection point of the  $2n$ th-derivative of entropy and the positive valley in the  $(2n + 1)$ th-derivative curve. For a  $2n$ th-order transition, the least sensitive inflection point in the  $(2n - 1)$ th-derivative of entropy together with the negative peak in the  $2n$ th-order derivative curve are utilized to locate the transition energy. The specialty of the first-order-like transition is that it can be distinguished from the back-bending region in the inverse temperature  $\beta(E) \equiv T^{-1}(E) = dS(E)/dE$  and the corresponding positive peak in the  $\gamma(E) = d\beta(E)/dE$  curve.

## 6.2 Results

### 6.2.1 Canonical and microcanonical analysis

First we discuss the results of canonical statistical analysis applied to our generic model. Heat-capacity curves as functions of temperature (Fig. 6.2(a)) are constructed using the time series of data collected in the multicanonical production run. At  $T \approx 0.34$ , broad prominent peaks, indicating the freezing transition, are identified for all simulated  $\eta$  values. At this transition, globular structures change to more compact crystalline or amorphous structures. For  $\eta = 0$ , an additional peak emerges at  $T = 0.11$ , suggesting the existence of a solid-solid transition. With increasing values of  $\eta$  the peak becomes more pronounced as it gradually shifts towards zero temperature and finally disappears when  $\eta \geq 0.1$ . However, the

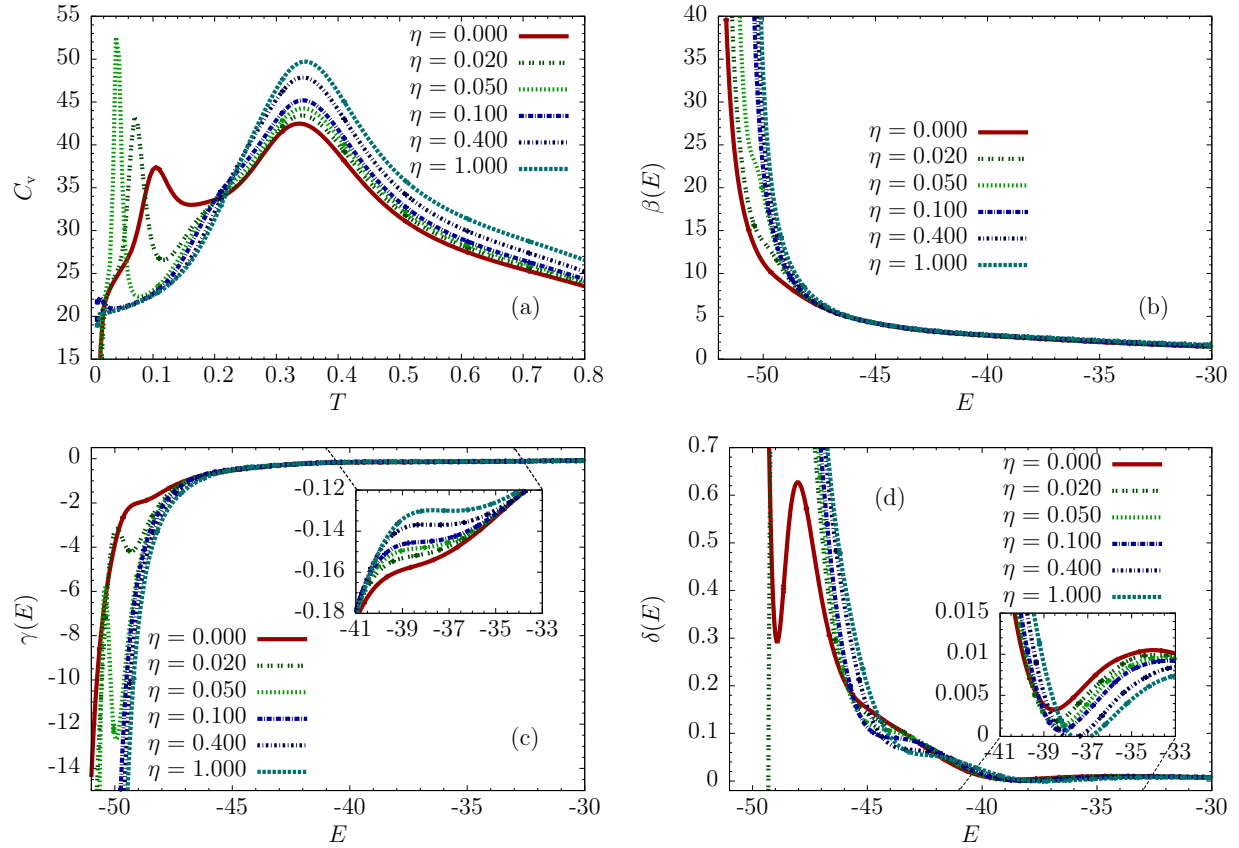


Figure 6.2: (a) Heat capacity  $C_v$ , (b) microcanonical inverse temperature  $\beta(E)$ , and (c,d) its first and second derivatives  $\gamma(E)$  and  $\delta(E)$ , respectively.

order of the individual transitions remains ambiguous and the broad peaks of the freezing transition may envelope several transitions which cannot be resolved by the methods of canonical analysis. Therefore we further examine the system using a more systematic and robust approach. One such method that has proven to reliably signal transitions is the microcanonical inflection-point analysis [8].

The microcanonical results are shown in Fig. 6.2(b-d) for six different values of  $\eta$ . Careful inspection of the first and second derivatives of  $\beta(E)$  in the energy region  $E \in [-41, -33]$  reveals that the broad peak in the canonical specific heat encloses two distinct transition signals; clear indication that the freezing transition is a two-step process. The first signal located at  $E \approx -44$ , is a fourth-order transition indicated by the corresponding least sensitive inflection point in  $\delta(E)$ . The second transition, found at  $E \approx -38$ , is of third order for  $\eta \leq 0.2$ , but it is classified as a second-order transition for higher values of the bond flexibility control parameter. In agreement with the canonical results, we have also identified signals corresponding to a solid-solid transition for values of  $\eta \leq 0.1$ . For  $\eta = 0.02$  and  $0.05$ , the negative-valued peaks in  $\gamma(E)$  at energies  $E = -49.7$  and  $-50.4$  respectively, indicate a second-order transition. The inflection point in  $\gamma(E)$  and the corresponding positive valley in  $\delta(E) = d\gamma(E)/dE$  at  $E = -48.92$  reveal that for  $\eta = 0.00$  the solid-solid transition is of third order.

The hyperphase diagram is constructed on the basis of the signals identified in the microcanonical analysis and plotted in Fig. 6.3. In the “gas” pseudophase at high energies, the polymer expands in free space and forms random-coil structures. As the energy decreases, the expanded chain undergoes a second-order collapse transition and enters the “liquid” pseudophase consisting mainly of globular structures. Passing the third/second-order transition associated with the nucleation process, the polymer enters the  $S_{ic}$  pseudophase in which incomplete icosahedral structures become dominant. Further decrease in energy weakens thermal fluctuations and allows for the formation of a stable surface layer. The transition

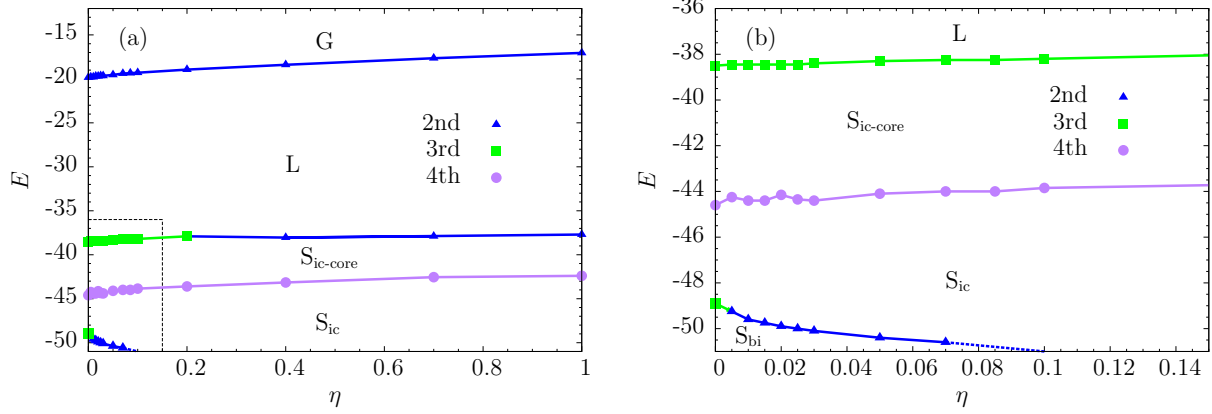


Figure 6.3: (a) Microcanonical hyper-phase diagram parametrized by energy and the bond flexibility control parameter  $\eta$ . Here, G, L, and S stand for “gas”, “liquid”, and “solid” structural phases, respectively. The  $S_{ic-core}$  pseudophase consists mostly of incomplete icosahedral structures.  $S_{ic}$  and  $S_{bi}$  incorporate compact icosahedral and bihexagonal structures, respectively. (b) Enlarged section detailing the low energy region for  $\eta < 0.15$ . The solid-solid transition line is extended by a dashed empirical line constructed based on the data provided by structural analysis.

associated with the surface formation process is of fourth order. Visual inspection of low-energy structures reveals that icosahedral geometries are dominant. However, for  $\eta \leq 0.1$ , the additional solid-solid transition suggests the existence of low-energy conformations with unexpected geometric properties. In order to examine the low-energy structures systematically, we carry out a careful structural analysis utilizing a suitable set of order parameters.

## 6.2.2 Structural analysis

Various order parameters, such as the number of monomer-monomer contacts, radius of gyration, or radial and angular distributions, have proven to provide valuable insight into the thermodynamic and structural properties of polymer systems. Based on the microcanonical

results in Fig. 6.3, we expect the existence of two solid phases when the strength of the bond flexibility parameter is sufficiently small ( $\eta \leq 0.1$ ). We aim to identify the dominant structures in the low-energy phases and to gather additional data supporting the existence of the solid-solid transition line. For this purpose, we employ a set of order parameters exploiting the symmetry properties of real spherical harmonics [44].

We define a polymer core to consist of monomers within a distance  $r_{\text{core}} < 1.25\sigma$  of the central monomer, which has been chosen to be nearest to the center of mass. Let  $\mathcal{C} = \{\vec{r}_1, \dots, \vec{r}_M\}$  be the coordinates of a core with  $M$  monomers. Various core geometries can be distinguished using the set of rotationally invariant order parameters

$$Q_l = \left[ \frac{4\pi}{2l+1} \sum_{m=-l}^l |\rho_{l,m}|^2 \right]^{1/2}, \quad (6.7)$$

where

$$\rho_{l,m} = \frac{1}{M} \sum_{i=0}^M Y_{l,m}(\vec{r}_i) \quad (6.8)$$

is the average of the real spherical harmonics evaluated at the locations of the core monomers.

The connection between the real and complex spherical harmonics is given by

$$Y_{lm} = \begin{cases} \frac{i}{\sqrt{2}} [Y_l^m - (-1)^m Y_l^{-m}] & \text{if } m < 0, \\ Y_l^m & \text{if } m = 0, \\ \frac{1}{\sqrt{2}} [Y_l^{-m} + (-1)^m Y_l^m] & \text{if } m > 0. \end{cases} \quad (6.9)$$

Using of the order of  $10^6$  polymer structures per value of  $\eta$ , we computed  $Q_l$  up to  $l = 6$  and found that  $Q_6$  can be used most effectively to resolve the geometries of the low-energy conformations. We present the results in the form of intensity plots in Fig. 6.4. The probability of detecting a structure with a specific value of the order parameter at an energy  $E$  is represented by shading; red indicating the maximum probability and black corresponding

to zero. In agreement with the microcanonical and canonical results, we detect a single solid phase for  $\eta > 0.1$ , corresponding to the narrow funnel in  $Q_6$  below the transition line at  $E \approx -43$ . The dominant structures in this region contain an icosahedral core which is typically found in the ground-state conformations of many short polymer chains. Below  $\eta = 0.1$ , the 15mer explores an additional solid phase, as indicated by the appearance of a second funnel centered around  $Q_6 \approx 0.41$ . Structures which populate this phase possess an unusual bihexagonal geometry which has also been recently found in longer chains. The energy at which both phases coexist agrees well with the microcanonical estimates for the solid-solid transition. Representative structures of both solid phases are shown in Fig. 6.5.

The shape of the bonded potential has undoubtedly a strong effect on the geometry of the ground state. Having identified the two dominant structure types, we may ask why the additional LJ term in the bonded potential eventually precludes the existence of the bihexagonal phase. The answer is readily obtained by comparing the average bond lengths for the icosahedral and bihexagonal structures. The bihexagon accommodates all monomers into a single shell allowing for a larger number of non-bonded interactions and consequently lower energy. However, the two six-monomer rings of the bihexagon contain significantly compressed bonds ( $r_{\text{bond}} \approx 0.88r_0$ ), which become energetically infeasible as  $\eta$  increases. In contrast, we find near-optimal bond lengths in the icosahedron ( $r_{\text{bond}} \approx r_0$ ), hence the “narrowing” of the bonded potential imposes no additional energetic penalty.

## 6.3 Summary

By means of multicanonical simulations of a generic model for elastic, flexible polymers, we have investigated the structural behavior of a 15-mer upon changing a model parameter  $\eta$  that controls the shape of the bonded potential. For small values of this parameter, a freezing transition into an icosahedral phase precedes a solid-solid transition into low-energy



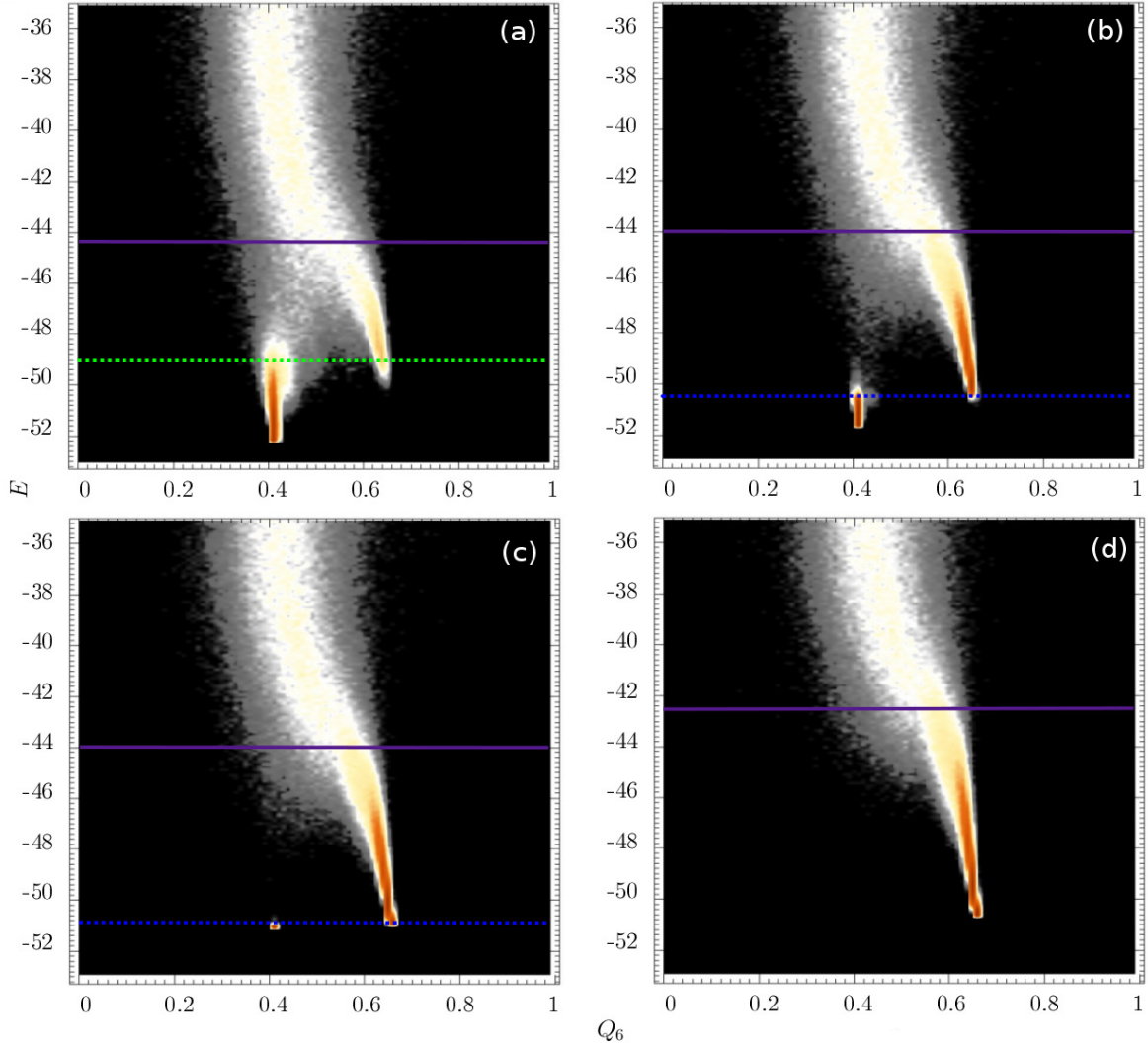


Figure 6.4: (a,b,c,d) Intensity plots of the  $Q_6$  order parameter for a 15mer with  $\eta = 0.00, 0.05, 0.10, 1.0$ . The shading indicates the probability of detecting a configuration with a given value of the order parameter, red being the maximum probability and black being the lowest. The freezing and the solid-solid transitions are indicated by solid and dashed horizontal lines respectively. For  $\eta \leq 0.1$ , the polymer has two distinct solid phases. In addition to the icosahedral phase ( $Q_6 \approx 0.65$ ) the polymer is found in the bihexagonal phase at low energies ( $Q_6 \approx 0.41$ ).

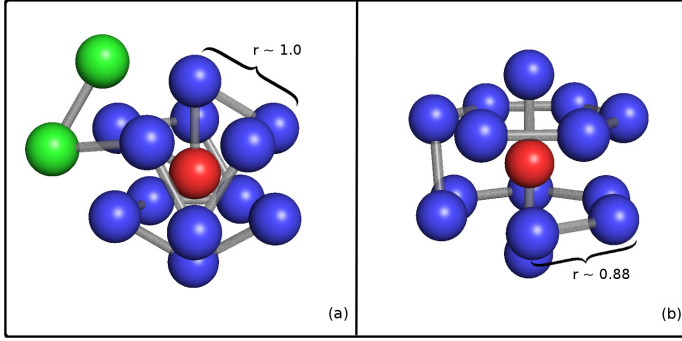


Figure 6.5: Two distinct low-energy structures of the elastic 15-mer. (a) Compact structure with a stable icosahedral core and two monomers displaced onto the incomplete second layer. (b) The bihexagon is the preferred ground-state geometry for  $\eta \leq 0.1$ .

states with bihexagonal geometry. The non-optimal bond lengths found in bihexagonal conformations cause a large energy penalty due to the “narrowing” of the bonded potential if  $\eta$  is increased. Hence only a single solid phase remains for  $\eta > 0.1$ , which is icosahedral. The striking consequences of a relatively small modification to the standard model of elastic, flexible homopolymers illustrate the importance of a careful choice of model parameters.

# Chapter 7

## Aggregation of Flexible Elastic Homopolymers

### 7.1 Introduction

### 7.2 Microcanonical analysis

#### 7.2.1 Subphases and subphase transitions

#### 7.2.2 Missing subphases and translational entropy

#### 7.2.3 Density effects on the latent heat

# Chapter 8

## Summary and Outlook

Table 8.1: Example of a table.  
[The contents of the table would go here.]

# Bibliography

- [1] M. Bachmann, *Thermodynamics and Statistical Mechanics of Macromolecular Systems* (Cambridge University Press, Cambridge, 2014).
- [2] H. H. Rugh, Phys. Rev. E **64**, 055101 (2001).
- [3] M. Kardar, *Statistical Physics of Particles*, (Cambridge University Press, New York, 2007).
- [4] R. K. Pathria, and P. D. Beale, *Statistical Mechanics*, (Elsevier, Oxford, 2011).
- [5] J. P. Sethna, *Statistical Mechanics: Entropy, Order Parameters, and Complexity*, (Oxford University Press, New York, 2006).
- [6] D. H. E. Gross, *Microcanonical Thermodynamics*, (World Scientific, Singapore, 2001).
- [7] P. M. Stevenson, Phys. Rev. D **23**, 2916 (1981).
- [8] S. Schnabel, D. T. Seaton, D. P. Landau, and M. Bachmann, Phys. Rev. E **84**, 011127 (2011).
- [9] D. P. Landau, and K. Binder, *A Guide to Monte Carlo Simulations in Statistical Physics*, (Cambridge University Press, Cambridge, 2000).
- [10] M. Kardar, *Statistical Physics of Fields*, (Cambridge University Press, New York, 2009).

- [11] W. Janke, Nuc Phys. B **63** A-C (1998).
- [12] F. Calvo, and P. Labastie, Chem. Phys. Lett. **247**, 395 (1995).
- [13] G. B. Arfken, *Mathematical Methods for Physicists*, (Elsevier, Oxford, 2013).
- [14] D. C. Rapaport, *The Art of Molecular Dynamics Simulation* (Cambridge University Press, New York, 2004).
- [15] M. E. Tuckerman, *Statistical Mechanics: Theory and Molecular Simulation* (Oxford University Press, New York, 2010).
- [16] S. I. Resnick, *Adventures in Stochastic Processes* (Birkhäuser, Boston, 2005).
- [17] N. Metropolis, A. W. Rosenbluth, M. N. Rosenbluth, and A. H. Teller, J. Chem. Phys. **21**, 1087 (1953).
- [18] R. H. Swendsen and J.-S. Wang, Phys. Rev. Lett. **57**, 2607 (1986).
- [19] C. J. Geyer, *Computing Science and Statistics: Proceedings of the 23rd Symposium on the Interface*, edited by E. M. Keramidas (Interface Foundation, Fairfax Station VA, 1991), 156.
- [20] K. Hukushima and K. Nemoto, J. Phys. Soc. Jpn. **65**, 1604 (1996).
- [21] K. Hukushima, H. Takayama, and K. Nemoto, Int. J. Mod. Phys. C **7**, 337 (1996).
- [22] T. Neuhaus and J. S. Hager, Phys. Rev. E **74**, 036702 (2006).
- [23] B. A. Berg and T. Neuhaus, Phys. Lett. B **267**, 249 (1991).
- [24] B. A. Berg and T. Neuhaus, Phys. Rev. Lett. **68**, 9 (1992).
- [25] W. Janke, Physica A **254**, 164 (1998).

- [26] B. A. Berg, *Comp. Phys. Commun.* **153**, 397 (2003).
- [27] B. A. Berg, *Markov Chain Monte Carlo Simulations* (World Scientific, Singapore, 2004).
- [28] M. Bachmann, *Phys. Scr.* **87**, 058504 (2013).
- [29] F. Wang and D. P. Landau, *Phys. Rev. Lett.* **86**, 2050 (2001).
- [30] F. Wang and D. P. Landau, *Phys. Rev. E* **64**, 056101 (2001).
- [31] T. Vogel, Y. W. Li, T. Wüst, and D. P. Landau, *Phys. Rev. Lett.* **110**, 210603 (2013).
- [32] A. M. Ferrenberg and R. H. Swendsen, *Phys. Rev. Lett.* **63**, 1195 (1989).
- [33] S. Kumar, D. Bouzida, R. H. Swendsen, P. A. Kollman, and J. M. Rosenberg, *J. Comput. Chem.* **13**, 1011 (1992).
- [34] P. Bézier, *Automatisme*, **13**, 391 (1968).
- [35] G. G. Lorentz, *Bernstein Polynomials* (University of Toronto Press, 1953).
- [36] M. Matsumoto and T. Nishimura, *ACM Trans. Model. Comput. Simul.* **8**, 1049-3301 (1998).
- [37] D. S. Sholl, *Density Functional Theory: A Practical Introduction* (John Wiley & Sons, Hoboken, New Jersey, 2009).
- [38] F. Schmid, *Theory and Simulation of Multiphase Polymer Systems: Handbook of Multiphase Polymer Systems*, edited by A. Boudenne, L. Ibos, Y. Candau, and S. Thomas (John Wiley & Sons Ltd, Chichester UK, 2011), 31.
- [39] D. J. Griffiths, *Introduction to Electrodynamics* (Prentice-Hall Inc., Upper Saddle River, New Jersey, 1999).

- [40] J. E. Lennard-Jones, Proc. Phys. Soc. **43**, 461 (1931).
- [41] R. B. Bird, C. F. Curtiss, R. C. Armstrong, and O. Hassager, *Dynamics of Polymeric Liquids*, 2nd ed. (Wiley, New York, 1987).
- [42] K. Kremer and G. S. Grest, J. Chem. Phys. **92**, 5057 (1990).
- [43] A. Milchev, A. Bhattacharya, and K. Binder, Macromolecules **34**, 1881 (2001).
- [44] J. P. Neirotti, F. Calvo, D. L. Freeman, and J. D. Doll, J. Chem. Phys. **112**, 10340 (2000).
- [45] T. Koci and K. Qi, proceedings of CCP2015 (2016).
- [46] M. P. Taylor, W. Paul, and K. Binder, J. Chem. Phys. **131**, 114907 (2009).
- [47] M. P. Taylor, W. Paul, and K. Binder, Phys. Rev. E **79**, 050801(R) (2009).
- [48] J. Gross, T. Neuhaus, T. Vogel, and M. Bachmann, J. Chem. Phys. **138**, 074905 (2013).
- [49] S. Schnabel, M. Bachmann, and W. Janke, J. Chem. Phys. **131**, 124904 (2009).
- [50] S. Schnabel, T. Vogel, M. Bachmann, and W. Janke, Chem. Phys. Lett. **476**, 201 (2009).
- [51] I. M. Lifshitz, A. Yu. Grosberg, and A. R. Khokhlov, Rev. Mod. Phys. **50**, 683 (1978).
- [52] A. R. Khokhlov, Physica A **105**, 357 (1981).
- [53] D. D. Frantz, J. Chem. Phys. **115**, 6136 (2001).
- [54] V. A. Mandelshtam and P. A. Frantsuzov, J. Chem. Phys. **124**, 204511 (2006).
- [55] T. Koci and M. Bachmann, Physics Procedia, **68**, 80-84 (2015).
- [56] C. Junghans, M. Bachmann, and W. Janke, J. Chem. Phys. **128**, 085103 (2008).



- [57] C. Junghans, M. Bachmann, and W. Janke, *Europhys. Lett.* **87**, 40002 (2009).
- [58] C. Junghans, W. Janke, and M. Bachmann, *Comp. Phys. Commun.* **182**, 1937 (2011).
- [59] J. P. Neirotti, F. Calvo, D. L. Freeman, and J. D. Doll, *J. Chem. Phys.* **112**, 10340 (2000).
- [60] F. Calvo, J. P. Neirotti, D. L. Freeman, and J. D. Doll, *J. Chem. Phys.* **112**, 10350 (2000).